VIRTUAL TESTING OF ADVANCED POLYMER COMPOSITE MATERIALS

Ana Andreia Pinheiro Durão Branco

Master's Thesis
Advisor: Prof. Dr. Pedro Ponces Camanho

U.PORTO
FEUP FACULDADE DE ENGENHARIA
UNIVERSIDADE DO PORTO

Mestrado Integrado em Engenharia Mecânica

July 17, 2015

Abstract

In this thesis, the validation of the models used to virtually predict inelastic deformation and fracture of advanced polymer composites is performed. Due to the complex response of the composite materials, a building block validation is followed making the analysis of growing complexity according to the specimen used.

Different damage mechanisms, namely matrix transverse cracking, fibre fracture and delamination, are analysed and the CFRP's response studied accordingly, with the help of Abaqus UEL (user subroutines) and VUMAT subroutines. The development of the mesh, the definition of the limit element size and the cohesive behaviour are presented.

As to validate the models, the IM7/8552 composite is virtually tested and the results compared with the experimental data obtained for unnotched and open hole specimens.

Resumo

Com esta tese, pretende efetuar-se a validação dos modelos usados para testar virtualmente a deformação inelástica e fratura de compósitos poliméricos avançados. Uma vez que se trata de um comportamento complexo, efetua-se uma validação em pirâmide, de forma a obter a resposta de provetes gradualmente mais complexos.

São estudados diferentes mecanismos de dano, nomeadamente fissuração transversal da matriz, fratura da fibra e delaminagem, com a ajuda do Abaqus UEL (subrotinas definidas pelo utilizador) e subrotinas VUMAT. O desenvolvimento da malha e a definição do comportamento coesivo e do tamanho crítico dos elementos são apresentados.

De forma a validar os modelos, o compósito IM7/8552 é virtualmente testado e os resultados obtidos são comparados com os dados experimentais dos provetes simples e de furo aberto.

Acknowledgements

To Prof. Dr. Pedro Camanho, supervisor of the thesis, for his patience and knowledge, for always making time to see me and for pushing me to do the best job possible. I could not ask for a better supervisor or a more supportive one.

To Giuseppe Catalanotti, postdoctoral researcher, for his tireless efforts teaching and encouraging me and for making me realise that even tough the subject at hand was challenging, clearance would come with time.

To Albertino Arteiro, for supplying the latest version of VUMAT and for his help analysing it.

To my friends, for their support and concern throughout this semester.

To my family, for always encouraging me when I was overwhelmed and for supporting me trough all my academic journey.

Contents

List of Tables

List of Figures

List of Abbreviations

Acronyms

2D Two-dimensional

3D Three-dimensional

4-ENF Four-Point End Notched Flexure

ASTM American Society for Testing and Materials

B-K Benzeggagh-Kenane

CDM Continuum Damage Model

CC Compact Compression

CFRP Carbon Fibre Reinforced Polymer

CT Compact Tension

DBB Double-Bearing Bolted

DBP Double-Bearing Pinned

DCB Double Cantilever Beam

DEC Double-Edge Cracked

DIC Digital Image Correlation

OHC Open Hole Compression

OHT Open Hole Tension

PAN Polyacrylonitrile

SBB Single-Bearing Bolted

SBP Single-Bearing Pinned

SCM Smeared Crack Model

UC Unnotched Compression

UD Unidirectional

UT Unnotched Tension

UEL User-defined Elements

Symbols

$\langle\cdot\rangle$ Macaulay operator;
$\boldsymbol{a}$ crack length;
$\boldsymbol{a_0}$ initial crack length;
$\boldsymbol{A_{IP}}$ area associated with the integration point;
$\boldsymbol{A_M}$ exponential softening law parameter;
$\boldsymbol{B}$ mode ratio;
$\boldsymbol{d}$ diameter;
$\boldsymbol{d_1}$ damage variable for longitudinal fiber failure;
$\boldsymbol{d_2}$ damage variable for transverse matrix cracking;
$\boldsymbol{d_6}$ damage variable influenced by longitudinal and transverse cracks;
$\boldsymbol{E_1}$ longitudinal Young's modulus;
$\boldsymbol{E_2}$ transverse Young's modulus;
$\boldsymbol{F_N}$ damage activation functions;
$\boldsymbol{g}$ fracture toughness ratio;
$\boldsymbol{g_M}$ energy dissipated per unit volume;
$\boldsymbol{G_c}$ fracture toughness;
$\boldsymbol{G_N}$ fracture toughness for the N failure mode;
$\boldsymbol{G_{12}}$ in-plane shear modulus;
$\boldsymbol{G^L_{1+}}$ energy dissipation per unit area in the linear softening response;
$\boldsymbol{G^E_{1+}}$ energy dissipation per unit area in the exponential softening response;
$\boldsymbol{I_1}$ first invariant;
$\boldsymbol{I_2}$ second invariant;
$\boldsymbol{I_3}$ third invariant;
$\boldsymbol{K_c}$ fracture toughness;
$\boldsymbol{K_{IC}}$ critical value of mode I stress intensity factor;
$\boldsymbol{K_{nn/ss}}$ stiffness coefficients;
$\boldsymbol{l}$ length;
$\boldsymbol{l^*}$ characteristic length of the finite element;
$\boldsymbol{l^*_{max}}$ maximum characteristic length of the finite element;
$\boldsymbol{P^\infty}$ ultimate load recorded;
$\boldsymbol{\bar{P}}$ normalized failure load;
$\boldsymbol{r_N}$ elastic domain thresholds;
$\mathbf{R}$ rotation matrix;
$\boldsymbol{S_L}$ shear strength;
$\boldsymbol{t}$ thickness;
$\boldsymbol{t_{n/s/t}}$ traction stresses in the cohesive response;
$\boldsymbol{t^0_{n/s/t}}$ traction stresses purely in the n/s/t direction;

$\boldsymbol{w}$ width;
$\boldsymbol{X_T}$ unnotched tensile strength;
$\boldsymbol{X_T^L}$ unnotched tensile strength of the laminate;
$\boldsymbol{X_C^L}$ unnotched compressive strength of the laminate;
$\boldsymbol{X_{PO}}$ pull-out stress;
$\boldsymbol{Y_T}$ transverse tensile strength.

Greek Letters

$\boldsymbol{\alpha_0}$ fracture angle;
$\boldsymbol{\alpha_{ii}}$ coefficients of thermal expansion;
$\boldsymbol{\alpha_1}$ transverse shear failure parameter;
$\boldsymbol{\alpha_2}$ in-plane shear failure parameter;
$\boldsymbol{\alpha_3^t}$ transverse tensile failure parameter;
$\boldsymbol{\alpha_3^c}$ transverse compressive failure parameter;
$\boldsymbol{\alpha_{32}^t}$ biaxial transverse tensile failure parameter;
$\boldsymbol{\alpha_{32}^c}$ biaxial transverse compressive failure parameter;
$\boldsymbol{\beta_{ii}}$ coefficients of hygroscopic expansion;
$\boldsymbol{\gamma}$ angle of mesh lines with crack direction;
$\boldsymbol{\delta_{ij}}$ Kroenecker delta;
$\boldsymbol{\delta_{n/s/t}}$ separations in the cohesive response;
$\boldsymbol{\Delta M}$ variation in moisture;
$\boldsymbol{\Delta T}$ variation in temperature;
$\boldsymbol{\varepsilon_{11}}$ strain in the longitudinal direction;
$\boldsymbol{\varepsilon_{22}^{cr}}$ scalar components of the strain tensor;
$\boldsymbol{\varepsilon_{c22}^{cr}}$ scalar components of cracking strain tensor;
$\boldsymbol{\varepsilon_c^{cr}}$ cracking strain projected in the coordinate system of the crack ;
$\boldsymbol{\eta}$ B-K material parameter;
$\boldsymbol{\eta^L}$ longitudinal friction coefficient;
$\boldsymbol{\lambda}$ equivalent displacement jump;
$\boldsymbol{\sigma^\infty}$ ultimate stress;
$\boldsymbol{\sigma_{11}}$ longitudinal stress;
$\boldsymbol{\sigma_{12}}$ shear stress;
$\boldsymbol{\sigma_{22}}$ transverse stress;
$\boldsymbol{\sigma^b}$ maximum stress obtained in bearing tests;
$\boldsymbol{\sigma_{exp}}$ maximum stress obtained in the experimental tests;
$\boldsymbol{\sigma_{num}}$ maximum stress obtained in the simulations;
$\boldsymbol{\tilde{\sigma}^\infty}$ remote failure stress;
$\boldsymbol{\tilde{\sigma}^m}$ stress tensor in the m coordinate system;
$\boldsymbol{\tilde{\tau}_{eff}^L}$ effective longitudinal stress;
$\boldsymbol{\tilde{\tau}_{eff}^T}$ effective transverse stress;
$\boldsymbol{\phi_0}$ initial misalignment angle;
$\boldsymbol{\phi_N}$ loading functions;
$\boldsymbol{\phi_R}$ angle originated by shear loading;
$\boldsymbol{\nu_{12}}$ major Poissons ratio;
$\boldsymbol{\omega_i^{cr}}$ scalar components of the displacement vector;

$\boldsymbol{\omega_f^m}$ equivalent displacement jump at failure under mixed-mode loading conditions.

1 Introduction

The reasoning behind the development of this thesis is the validation of the models, criteria and routines previously developed, which were born out of the growing interest in virtually predicting the inelastic deformation and fracture of advanced polymer composites. Numerical analysis arises from the need to reduce product development time and costs, leading to more competitive products needed in high performance and low weight structures.

To design and certificate complex composite structures, accurate strength prediction methods based on analysis models are required. The methods in question are review here in detail having in mind that imminently virtual testing of composite structures will replace some mechanical testing; however, this methodology is still evolving.

Due to the complex response of composite materials, there is a need for a well-planned test program when predicting the structural modes of failure and that is why a building block validation is followed according to figure 1. The motivation behind the use of this method is the validation of analysis models using specimens with growing complexity levels.

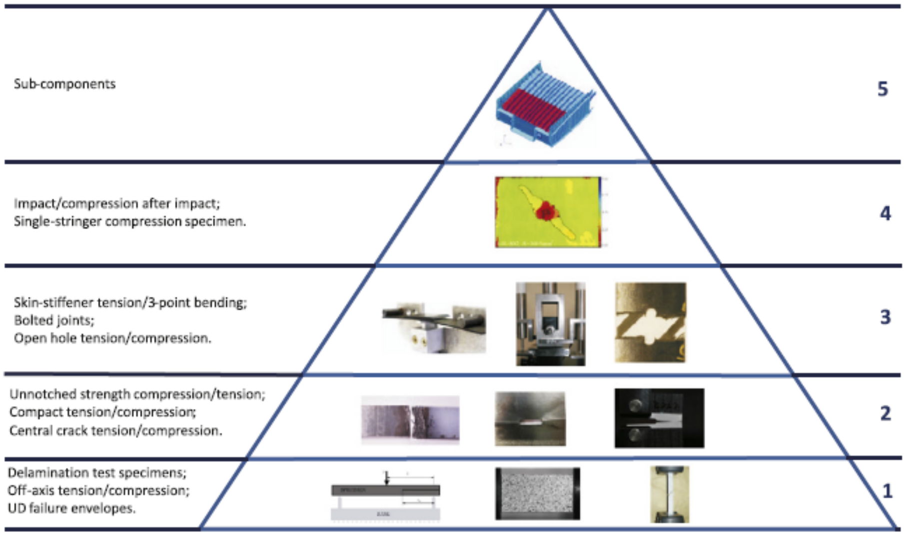

Figure 1: Suggested pyramid for building-block validation. [15]

The collapse of a composite structure is caused by the evolution of different damage mechanisms, namely matrix transverse cracking, fibre fracture and delamination. The exact sequence of failure mechanisms depends on the loading, geometry, lay-up and stacking sequence.

The models proposed to predict the onset and propagation of the different damage mechanisms are implemented using Abaqus UEL (user subroutines) and VUMAT subroutines and the reasoning behind the development of the mesh and the limit element size is presented.

The thesis is organized in five different chapters: chapter 2 describes the literature review performed on the Continuum Damage Model and the Smeared Crack Model; chapter 3 describes the experimental tests previously performed to measure the material properties needed for the routines; chapter 4 shows the numerical results and how they compare to the experimental data for IM7/8552 under tensile and compressive loading; the last chapter presents the main conclusions and suggestions for future work.

2 Literature Review

This chapter is mainly divided in two parts, the first part reviewing the two-dimensional models and the second part reviewing the three-dimensional models, which would both be later on implemented in the user routines for the numerical simulations.

2.1 2D Continuum Damage Model

Micro-mechanical models are ideal to design the material; they are not, however, suitable for structural analysis. In order to accomplish a model that gathers the advantages of both methods, arises the need to create a model that links the micro and macro-mechanical scale.

2.1.1 Constitutive Model

When working with materials that accumulate damage before collapse, which is the case of advanced composites, fracture mechanics is not a sufficient enough method to predict ultimate failure; especially when it comes to multi-directional laminates, since they are able to sustain a significant amount of damage before collapse. Therefore, alternative solutions must be explored [30].

Simplified models may be implemented, however, they do not have a satisfactory response when it comes to analysing materials with quasi-brittle failure behaviour under general loading scenarios.

As an alternative, non-linear constitutive models may be implemented. This type of Continuum Damage Models allows the analysis of damage from its onset to the final collapse, considering every ply as a homogenized material.

The model under review in this subsection has the advantage of working with very simple parameters which can be obtained from standard test methods. Another complementary advantage is related to the fact that these parameters are ply-based characteristics, which means that they do not demand alterations every time the lay-up of the composite is redefined.

Another feature inherent to the model that is important to highlight is that it accounts for crack closure effects under load reversal and therefore, allows the study of non-loading where this phenomenon has an important role.

One of the main advantages of the developed model is that it guarantees computational efficiency due to the fact that it can be integrated explicitly, which allows its use for large scale computations. However, the model under consideration does not allow the prediction of delamination, it focuses only on intralaminar failure such as matrix cracking and fibre fracture.

This method focuses on four different types of failure: transverse and longitudinal, tension and compression.

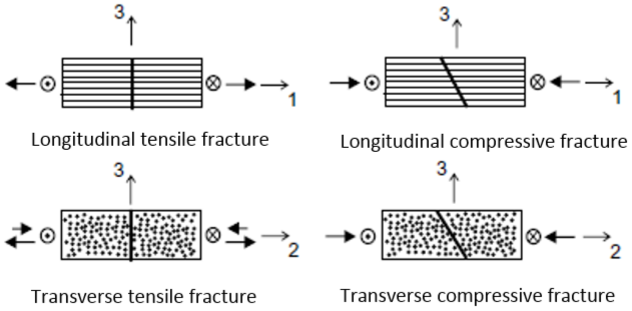

Figure 2: Different types of fracture considered in the model. [30]

Analysing in detail the structure of the model, one needs to acknowledge different parts: the constitutive law, the damage activation, the damage evolution and finally the softening constitutive law.

In order to define the constitutive law, it needs to be ensured that the irreversibility of the damage process is respected. With this in mind, a scalar function (complementary free energy density - G) is defined, insuring that it is positive definite and that it is zero at the origin when it comes to the stresses:

$$\boldsymbol{G = \frac{\sigma_{11}^2}{2(1-d_1)E_1} + \frac{\sigma_{22}^2}{2(1-d_2)E_2} - \frac{\nu_{12}}{E_1}\sigma_{11}\sigma_{22} + \frac{\sigma_{12}^2}{2(1-d_6)G_{12}}}$$
$$\boldsymbol{+(\alpha_{11}\sigma_{11} + \alpha_{22}\sigma_{22})\Delta T + (\beta_{11}\sigma_{11} + \beta_{22}\sigma_{22})\Delta M}$$

Like it was previously mentioned, the properties utilized here are at the level of each unidirectional lamina; $\boldsymbol{E_1, E_2, \nu_{12}, G_{12}}$, the in-plane elastic orthotropic properties; $\boldsymbol{\beta_{11/22}}$ are coefficients of hygroscopic expansion and, also involved in the definition of the constitutive law, are $\boldsymbol{\alpha_{11/22}}$, coefficients of thermal expansion. The variables $\boldsymbol{\Delta M}$ and $\boldsymbol{\Delta T}$ are the differences in temperature and moisture, respectively, compared to reference values. The representative volume to which the constitutive equations are applied must be larger than the diameter of the fibre.

Regarding the three scalar variables $\boldsymbol{d_1, d_2}$ and $\boldsymbol{d_6}$, they correspond to different damage variables which represent different types of damage in action: longitudinal fiber failure ($\boldsymbol{d_1}$), transverse matrix cracking ($\boldsymbol{d_2}$) and damage influenced by longitudinal and transverse cracks ($\boldsymbol{d_6}$). These variables allow the definition of the domain of elastic response, essential for the development of the damage model.

In order to track whether the kind of damage mechanisms in action is due to compression or tension, fiber failure or matrix cracking, the damage modes are defined in the following way:

$$\boldsymbol{d_1 = d_{1+}\frac{\langle \sigma_{11}\rangle}{|\sigma_{11}|} + d_{1-}\frac{\langle -\sigma_{11}\rangle}{|\sigma_{11}|}}$$

$$\boldsymbol{d_2 = d_{2+}\frac{\langle \sigma_{22}\rangle}{|\sigma_{22}|} + d_{2-}\frac{\langle -\sigma_{22}\rangle}{|\sigma_{22}|}}$$

Knowing that $\boldsymbol{\langle x\rangle}$ is the Macaulay operator, and so, $\boldsymbol{\langle x\rangle = (x + |x|)/2}$.

2.1.1.1 Damage activation functions

To determine the type of damage initiated, four damage activation functions, $\boldsymbol{F_{1+}, F_{1-}, F_{2+}, F_{2-}}$, are defined. These functions are based on the LaRC03 and LaRC04 criteria; the latter being used selectively, due to its increasing computational needs. These criteria do not require curve-fitting parameters and have no restrictions regarding loading combinations [11].

Graphically, the four damage activation variables represent different surfaces that constrict the elastic domain, a space where the material is linear elastic and when one becomes positive, the material's response is no longer elastic and there is damage evolution. The functions $\boldsymbol{F_N}$ are defined according to the following expressions:

$$\boldsymbol{F_{1+} = \phi_{1+} - r_{1+} \leqslant 0}$$

$$
\begin{aligned}
\boldsymbol{F_{1-}} &= \boldsymbol{\phi_{1-} - r_{1-} \leqslant 0} \\
\boldsymbol{F_{2+}} &= \boldsymbol{\phi_{2+} - r_{2+} \leqslant 0} \\
\boldsymbol{F_{2-}} &= \boldsymbol{\phi_{2-} - r_{2-} \leqslant 0}
\end{aligned}
$$

Where $\boldsymbol{\phi_N}$ represents the loading function that depends on strain tensor and material constants and $\boldsymbol{r_N}$ represent the elastic domain thresholds which are related to the damage variables ($\boldsymbol{d_N}$) and take the value of 1 when the material is undamaged and increase with damage.

2.1.1.1.1 Damage activation functions in longitudinal fracture

For longitudinal tension, a non-interactive strain criterion based on the LaRC04 criterion is used to define the loading function as shown:

$$\boldsymbol{\phi_{1+} = \frac{E_1}{X_T}\varepsilon_{11}}$$

However, in longitudinal compression, since there is damage onset in the matrix, a loss of lateral support for the fibres leads to a formation of a kink band. In these conditions, the loading function is established according to the LaRC03 criterion and takes form as:

$$\boldsymbol{\phi_{1-} = \frac{\langle |\tilde{\sigma}^m_{12}| + \eta^L \tilde{\sigma}^m_{22} \rangle}{S_L}}$$

Where $\boldsymbol{\eta^L}$ represents the longitudinal friction coefficient as determined in [24] and the $\boldsymbol{\tilde{\sigma}^m}$ represents the stress tensor in the coordinate system of the misaligned fiber plane. This criterion's development asks for the input of the misalignment angle of the fibres which is a function of the applied stress. However, as a simplification, the model uses a constant angle that corresponds to the one in a pure longitudinal compression scenario.

2.1.1.1.2 Damage activation functions in transverse fracture

Depending on the type of loading that leads to transverse fracture, the material might crack perpendicularly to the mid-plane of the ply ($\boldsymbol{\alpha_0 = 0^\circ}$) or with a crack plane angle of $\boldsymbol{53^\circ}$. The cases described correspond respectively to in-plane shear stresses combined with transverse tensile stresses or to in-plane shear stresses combined with small transverse compressive stresses and high transverse stresses.

Using the LaRC04 criterion, both cases are analysed, leading to three different expressions for the loading functions as presented:

$$\phi_{2+} = \sqrt{(1-g)\frac{\tilde{\sigma}_{22}}{Y_T} + g\left(\frac{\tilde{\sigma}_{22}}{Y_T}\right)^2 + \left(\frac{\tilde{\sigma}_{12}}{S_L}\right)^2} \qquad if \;\; \tilde{\sigma}_{12} \geqslant 0$$

$$\phi_{2+} = \frac{1}{S_L}\langle|\tilde{\sigma}_{12}| + \eta^L \tilde{\sigma}_{22}\rangle \qquad if \;\; \tilde{\sigma}_{12} < 0$$

For $\alpha_0 = 0°$ and where $g = \frac{G_{Ic}}{G_{IIc}}$, i.e. it represents the fracture toughness ratio.

$$\phi_{2-} = \sqrt{\left(\frac{\tilde{\tau}^T_{eff}}{S_T}\right)^2 + \left(\frac{\tilde{\tau}^L_{eff}}{S_L}\right)^2} \qquad if \;\; \tilde{\sigma}_{12} < 0$$

For $\alpha_0 = 53°$ and where $\tilde{\tau}^{T/L}_{eff}$ represents the effective stresses defined in [33].

Under transverse fracture where compression is principal, the fracture angle is indeed approximately $53°$ in carbon-epoxy composites. However, with increasing in-plane shear, the angle diminishes, going through $40°$ and ultimately reaching $0°$. With computational efficiency in mind, the model allows only discrete values of $53°$ and $0°$,

2.1.1.2 Damage evolution

Damage evolution is defined by the *Kuhn-Tucker* conditions that can be represented as:

$$r_N \geqslant 0; \quad F_N \leqslant 0; \quad r_N F_N = 0$$

This means that while F_N is negative, the material has an elastic behaviour but when it reaches 0 and other conditions are met, there is damage evolution.

Even though during damage evolution there is an active elastic domain being analysed, the model still accompanies the evolution of the other elastic domains; always assuming that transverse and longitudinal domains are never coupled.

2.1.1.3 Softening laws

In order to ensure a safe implementation of the softening constitutive equations, the Ba*ž*ants crack band model is implemented for each intralaminar failure mode in question with the addition of a definition of the maximum size of the finite elements.

This is implemented regularizing the computed dissipated energy with the use of a characteristic dimension of the finite element and the fracture toughness [28], which leads to:

$$\boldsymbol{g_M = \frac{G_M}{l^*}, M = 1\pm, 2\pm, 6}$$

Where $\boldsymbol{G_M}$ is the fracture toughness, $\boldsymbol{g_M}$ is the energy dissipated per unit volume, and $\boldsymbol{l^*}$ is the characteristic length of the finite element. For square elements, the characteristic element length can be approximated by the following expression:

$$\boldsymbol{l^* = \frac{\sqrt{A_{IP}}}{cos(\gamma)}}$$

Where $|\gamma| \leq \boldsymbol{45^\circ}$ is the angle of the mesh lines with the crack direction and $\boldsymbol{A_{IP}}$ is the area associated with each integration point.

The crack band model uses an approximation to represent the failure process zone by a damaged finite element zone with the width of one element as to achieve an appropriate response to complex mechanisms in large structures.

As soon as one of the $\boldsymbol{F_N}$ is activated, the damage evolution laws are triggered in order to represent the cohesive response which is linear until the stress reaches the pull-out stress, $\boldsymbol{X_{PO}}$, and the corresponding energy dissipation per unit area is $\boldsymbol{G^L_{1+}}$. As the strains continue to increase, the softening response follows an exponential law and the energy dissipated per unit area is $\boldsymbol{G^E_{1+}}$ [31] as can be seen in figure 3.

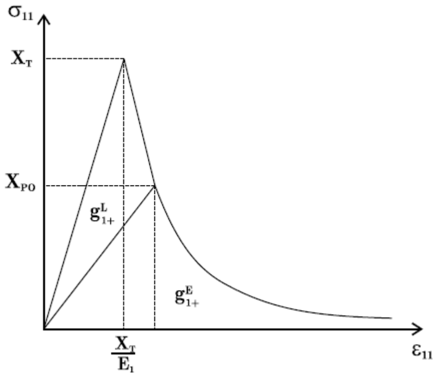

Figure 3: Example of damage evolution using both linear and exponential laws. [31]

The exponential damage evolution laws proposed are expressed as follows:

$$\boldsymbol{d_M = 1 - \frac{1}{f_N(r_N)} exp\{A_M[1 - f_N(r_N)]\}}$$

Where the function $\boldsymbol{f_N(r_N)}$ is selected to force the softening of the constitutive relation and $\boldsymbol{A_M}$ is a parameter that defines the exponential softening law.

In order for the constitutive model [31] not to lead to a local snap-back in the stress-strain relation, a maximum size is defined for the elements. In other words, the elastic energy of an element at the onset of localization, which is $\boldsymbol{X_M^2(l^*)^2t/(2E_M)}$ with $\boldsymbol{M = 1\pm, 2\pm, 6}$, must be lower than or equal to the fracture energy, $\boldsymbol{G_M l^* t}$, where $\boldsymbol{t}$ is the ply thickness. Therefore, the maximum size for the finite element for each damage law M is:

$$\boldsymbol{l^* \leq \frac{2E_M G_M}{X_M^2}, M = 1\pm, 2\pm, 6}$$

Where $\boldsymbol{E_M, G_M}$ and $\boldsymbol{X_M}$ are the Young's modulus, fracture energies and strengths, respectively.

When the direction of the crack is known in advance, it is recommended that the mesh be aligned with it since the crack tends to propagate aligned with the element's borders.

With the evolution law defined, the integration of the rate at which the energy is dissipated associated with the definition of characteristic length leads to proof of the independence from mesh size.

In addition, it is important to refer that only half of the specimen is modelled in order to reduce computation efforts. Also, since a maximum element size is defined but not always possible to enforce, a strategy is defined as to automatically lower the strength of the bigger elements, keeping the fracture toughness constant.

2.2 3D Constitutive Models

The model under review in this section uses a three-dimensional Smeared Crack Model to predict the onset and propagation of failure in transverse cracking and a modification of the previously described 2D model ([30] and [31]) to represent the longitudinal failure. The main concern here is to analyse more complicated stress states and to account for the plastic deformation of the polymer resin that precedes the cracking of the plies [15].

The validation process is also more complete, applying a building-block validation model of five levels of growing complexity. This approach guarantees that costs are minimized while performance objectives are met, since smaller and cheaper specimens are tested first, and only when technology risks are assessed, does the level of complexity of the tests increase.

In order to predict compressive and tensile transverse matrix cracking, the model proposes a 3D invariant-based criterion that is formulated directly from the yield function presented in [40]. This formulation defines **a**, the preferred direction in transversely isotropic materials, around which the material's response is invariant with respect to arbitrary rotations.

There is also the need to specify a structural tensor of transverse isotropy, **A**, representing the material's intrinsic characteristic direction [14]. Having defined all the elements, the failure indexes $\boldsymbol{\phi_{2\pm}}$ can now be reached according to the expressions presented in [14] that lead to:

$$\boldsymbol{\phi_{2\pm} = \alpha_1 I_1 + \alpha_2 I_2 + \alpha_3 I_3 + \alpha_{32} I_3^2 \leq 1}$$

With: $\boldsymbol{\alpha_3 = \alpha_3^t, \alpha_{32} = \alpha_{32}^t}$ if $\boldsymbol{I_3 > 0}$ and $\boldsymbol{\alpha_3 = \alpha_3^c, \alpha_{32} = \alpha_{32}^c}$ if $\boldsymbol{I_3 \leq 0}$.

The proposed failure criteria allows for the study of failure under biaxial stress states to be made and the six failure parameters ($\boldsymbol{\alpha_1}, \boldsymbol{\alpha_2}, \boldsymbol{\alpha_3^t}, \boldsymbol{\alpha_3^c}, \boldsymbol{\alpha_{32}^t}$ and $\boldsymbol{\alpha_{32}^c}$) are functions of the transverse and in-plane shear strengths, the transverse tensile and compressive strengths, and the biaxial transverse tensile and compressive strengths [14].

The criterion defined provides feasible predictions for the different load cases analysed.

Once defined the onset of transverse failure, it is now necessary to simulate the cracks under general loading. Since the orientation of the crack plane depends on the stress state, it is not possible to use cohesive zone models and so a Smeared Crack Model based on the work presented in [28] is used.

2.2.1 Damage Model for transverse fracture - SCM

A Smeared Crack Model is a constitutive model specifically developed for quasibrittle materials in which the total strain is considered a summation of two parts: the strain correspondent to the deformation of the uncracked material and the additional deformation due to the opening of cracks.

$$\boldsymbol{\varepsilon} = \boldsymbol{\varepsilon_e} + \boldsymbol{\varepsilon_c} = \boldsymbol{\varepsilon_e} + \mathbf{R} \cdot \boldsymbol{\varepsilon_c^{cr}} \cdot \mathbf{R}^{\boldsymbol{T}}$$

Where $\boldsymbol{\varepsilon_c^{cr}}$ is the cracking strain projected in the coordinate system of the crack and $\mathbf{R}$ is the rotation matrix, whose components are defined by the failure criteria [15].

As mentioned before, the transverse fracture under compressive loading leads to a fracture angle that, in the case of a simple stress state in carbon-epoxy composites, is $\mathbf{53^\circ}$. However, in this case, a more complex stress states is being analysed and thus the use of a rotation matrix that calculates the angle of fracture at the onset of the crack. Further along in the model, that angle is considered a constant, i.e., a rotating crack is not analysed.

At this point, a projection of the tractions acting on the fracture plane onto the crack frame is made and now the displacement jumps must be related to the tractions. This correlation is done using a cohesive law based on that developed by Turon [39] but bearing in mind that the linear softening cohesive law must be adapted to the Smeared Crack Model. This said, the tractions acting on the fracture plane are defined as:

$$t_i^{cr} = \left(\frac{1-d}{d}\right)\frac{\omega_i^{cr}}{\omega_i^{m}}\bar{t}_i^{cr} - \delta_{i2}\frac{\langle -\omega_2^{cr}\rangle}{|\omega_2^{cr}|}\left[\left(\frac{1-d}{d}\right)\frac{\omega_i^{cr}}{\omega_f^{m}}\bar{t}_i^{cr} - E_2(\varepsilon_{22}^{cr} - \varepsilon_{c22}^{cr})\right]$$

Knowing that:
δ_{ij}: Kroenecker delta;
ω_f^m: equivalent displacement jump at failure under mixed-mode loading conditions;
ω_i^{cr}: scalar components of the displacement vector;
ε_{22}^{cr} and ε_{c22}^{cr}: scalar components of strain and cracking strain tensors, respectively;
$\langle\cdot\rangle$: Macaulay operator defined before.

The damage variable (d) is obtained using a loading function defined as $\mathscr{L}(\omega^{cr}) = min\left\{\frac{\lambda}{\omega_f^m}, 1\right\}$ where λ is the equivalent displacement jump.

To predict the mixed-mode interlaminar fracture toughness of composite laminates, the B-K criterion [13], a criterion based on energy release rate, is used. Both the linear criterion and the B-K criterion would be applicable here, however, the latter provides additional flexibility since it has an additional material parameter (η) [15]. The development of this criterion occurs as such:

$$G_c = G_{ic} + AB^{\eta}$$

With the mode ratio being $B = \frac{\bar{t}_s^{cr}\beta}{\beta(\bar{t}_s^{cr} - \bar{t}_2^{cr}) + \bar{t}_2^{cr}}$, the mixed-mode fracture toughness being $G_c = \frac{2(G_{ic} + AB^{\eta})}{\bar{t}^{cr}}$ and $A = G_{IIc} - G_{Ic}$.

2.2.2 Damage Model for longitudinal fracture - CDM

Since the SCM does not permit the representation of some mechanisms of longitudinal failure - non matrix dominated ones - the same failure criterion as in the 2D model [30] must be implemented in this field with some modifications.

The function that predicts longitudinal tensile fracture is the maximum strain criterion:

$$\phi_{1-} = \frac{\varepsilon_{11}}{\varepsilon_1^T}$$

When compressive loading is longitudinally applied, the effects of fiber kinking are relevant and must be predicted. In order to do so, the hypothesis put forward by Argon in [9] is used to develop the model. The hypothesis assumes that kink bands are triggered by localized matrix failure in the vicinity of misaligned fibres [9].

It is assumed that the angle $\boldsymbol{\theta}$ represented in figure 4 is a function of the stress state and that the kinking plane is defined by the shear stresses that act on the 23 plane [20]. The angle $\boldsymbol{\theta}$ can be calculated as $\boldsymbol{\theta = arctan(\tau_{13}/\tau_{12})}$. Once the kinking-angle ($\boldsymbol{\phi}$) is found, the stresses should be rotated to the misalignment frame - new coordinate system.

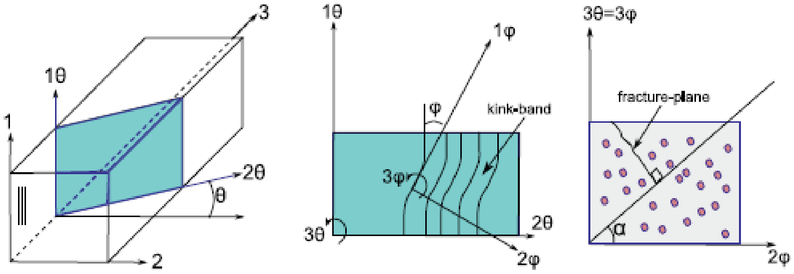

Figure 4: Representation of the different coordinate systems [20].

Once again, the invariant-based failure criteria is used but now the invariants are defined in the misalignment frame as follows:

$$\boldsymbol{I_1 = \frac{1}{4}\sigma_{11}^2 \sin^4 \phi}$$

$$\boldsymbol{I_2 = \sigma_{11}^2 \sin^2 \phi \cos^2 \phi}$$

$$\boldsymbol{I_3 = \sigma_{11}^2 \sin^2 \phi}$$

In order to find the angle $\boldsymbol{\phi}$ for plane stress states, [23] used a combination of Argon's approach and LaRC02 and 03 failure criteria; being the total misalignment $\boldsymbol{\phi}$ a summation of an initial constant misalignment angle $\boldsymbol{\phi_0}$ (that represents manufacture defects and imperfections in the materials) and a $\boldsymbol{\phi_R}$ angle that is originated by the shear loading applied and depends on the shear constitutive law. The misalignment angle can then be obtained as:

$$\boldsymbol{\phi = \phi_0 + \phi_R}$$

When it comes to damage evolution, just as in the 2D model analysed in another section, a bi-linear softening law is required, so as not to over predict the peak load in fiber dominated failure.

Once again, the characteristic length ($\boldsymbol{l^*}$) is used in this model as to ensure the independence from the element size. The same $\boldsymbol{l^*}$ will be considered in both transverse and longitudinal modes.

A consequence of the increasing complexity of the validation models is that, with different specimens, different specifications arise. For example, in the case of specimens with geometrical discontinuities, the stress tensor has non-zero out-of-plane components which may lead to delamination and therefore, the use of cohesive finite elements or surfaces must be implemented in-between the plies.

3 Experimental tests on carbon fibre reinforced polymers

3.1 Material and Lay-up Characterization

The materials under review in this section are the T800/M21 and the IM7/8552 composites. In a first approach, the specifications of the materials will be supplied.

3.1.1 T800/M21

The material in question has the commercial name of HexPly®M21/34%/UD134/T800S/600mm and it is a pre-impregnated carbon/epoxy unidirectional (UD) tape material, supplied by Hexcel. It is an epoxy reinforced by intermediate modulus carbon UD fibres, M21 is the resin type and 34% its weight content. The 134/T800S is the reinforcement reference and T800S represents the intermediate modulus carbon fiber. It possesses a high performance, tough epoxy matrix and its main use is in the aerospace industry since it has an excellent damage tolerance, especially at high energy impacts [26].

The material is supplied with unidirectional or woven carbon glass fibres and is developed as a controlled flow system to operate in environments up at **121**°C. It is best suited to press or autoclave cure so as to obtain optimum mechanical performance from the cured composite ([8] and [4]) and, after that process, it possesses a nominal ply thickness of 0.125 mm.

3.1.2 IM7/8552

HexTow®IM7/8552 carbon fiber is a continuous unidirectional laminate, capable of high performance, with an intermediate modulus and a Polyacrylonitrile (PAN) based fiber, composite material supplied as a pre-impregnated tape.

After the laying-up, the material was cured according to the manufacturer's specifications, with temperature stages of **110**°C during one hour, followed by temperatures of **180**°C for two hours and a pressure of 7 bar was applied during the duration of the cycle. The heating and cooling rates were **3**°C/min.

The fiber volume fraction was measured with image processing techniques resulting in an average value of 59.1%. The nominal thickness of the cured ply is 0.125 mm.

The two materials under analysis have different ply properties, which can be obtained using Standard Test Methods such as [3] and [8] and can be seen in table 1, presented below.

Table 1: Material properties for IM7/8552 and T800/M21.

Property	IM7/8552	T800/M21
	Ply elastic Properties	
Longitudinal Young's Moduli:	$\boldsymbol{E_1 = 171.4\ GPa}$	$\boldsymbol{E_1 = 172\ GPa}$
Transverse Young's Moduli:	$\boldsymbol{E_2 = 9.1\ GPa}$	$\boldsymbol{E_2 = 8.9\ GPa}$
Shear Moduli:	$\boldsymbol{G_{12} = 5.3\ GPa}$	$\boldsymbol{G_{12} = 5.0\ GPa}$
Poisson's ratios:	$\boldsymbol{\nu_{12} = 0.3\ GPa}$	$\boldsymbol{\nu_{12} = 0.32\ GPa}$

To perform experimental tests on materials with different lay-ups, multidirectional laminates were manufactured both in T800/M21 and in IM7/8552. With this in mind, specimens were then fabricated with stacking sequences as show in Table 2.

Table 2: Ply orientation of the various lay-ups.

Composite	Lay-up	Ply orientation
T800/M21	0	$\boldsymbol{[90/0]_{8s}}$
	1	$\boldsymbol{[(90/45/0/-45]_{3s}}$
	2	$\boldsymbol{[90_2/0_2/45_2/-45_2/90/0/45/-45]_s}$
IM7/8552	3	$\boldsymbol{[90/0]_{8s}}$
	4	$\boldsymbol{[0/45/90/-45]_s}$
	5	$\boldsymbol{[90/0/\pm 45]_{3s}}$

Following a building-block validation, two levels of experimental tests with growing complexity were analysed with the types of specimens enumerated in figure 5.

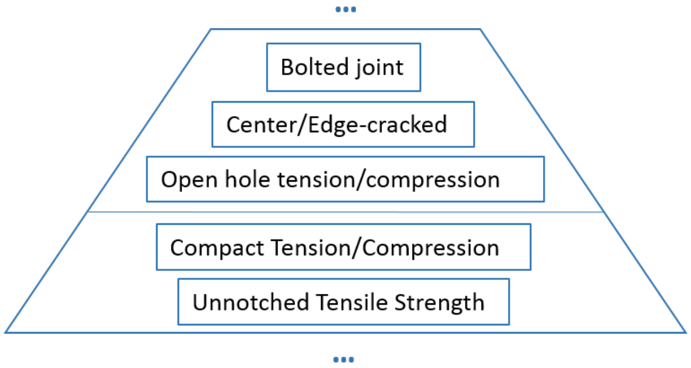

Figure 5: Levels 2 and 3 of the building-block validation and respective specimens.

3.2 Unnotched strength

Specimens made out of the T800/M21 composite material with nominal dimensions of 23x7x1.5 mm3 (length x width x thickness) were cut on a water-cooled diamond saw. All specimens were equipped with one linear strain gauge of the type HBM 1-LY11-1.5/350 at the specimen centre. Friction between the TC-inserts and the specimen's end-surface was reduced by applying a thin layer of lubricant.

The quasi-static tests were performed on a MTS-810 servohydraulic test machine. For data acquisition, the load cell of the test machine and the specimen strain gauge were connected to a HBM Spider-8 data acquisition system.

The shape of the specimens is defined according to ASTM Standard D 3039 [8] for tension and ASTM Standard D6484 [7] for compression and its basic geometry can be seen in figure 6.

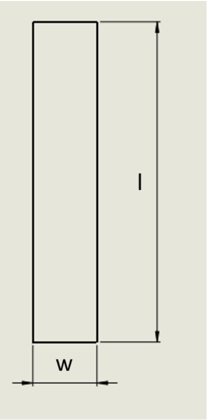

Figure 6: Geometric representation of the specimen for unnotched strength experiments.

Both lay-up 1 and 2 were tested, three specimens of each laminate in order to later on calculate the mean of the ultimate stress reach in the tests. The dimensions of the specimens developed are given in table 3.

Table 3: Dimensions of the different specimens.

Lay-up	Specimen	l [mm]	w [mm]	thickness [mm]
1 and 2	Tension	250	25	3.2
	Compression	305	25	3.2

3.2.1 Tensile tests

In order to perform the tensile experiment, the strain needs to be measured and to do so, strain gauges were placed at the center of the specimens in a vertical position using M-Bond 200 adhesive. The placement of the instruments in this case has no influence since the tension field here is uniform. The data gathered with the devices is then processed with the Spider 8 data acquisition system.

The specimens were experimented on in an MTS servo hydraulic testing machine and with a LoadCell-100 KN, which allow the recording of the progressive loads and consecutive failure stress - $\boldsymbol{X_L^T}$ defined.

As to validate the Aramis Digital Image Correlation (DIC) system, the back surface of the specimens was prepared allowing the achievement of comparable results of the two different metrological systems used. In figure 7, the set-up for the tensile tests can be seen.

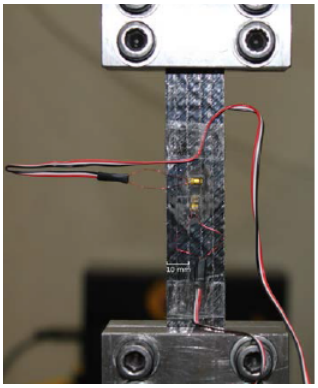

Figure 7: Photograph of the test set-up for the UT specimens [11].

3.2.2 Compressive tests

The compressive experiments were performed by the MTS servo hydraulic testing machine with a 100 KN LoadCell, according to the ASTM Standard D6484 [7]. The materials experimented on were the same as in the tensile tests, which means, three specimens of lay-up 1 and 2 were tested.

Both strain gauges and the Aramis DIC were utilized as to validate the latter; however, in this particular test, different specimens were equipped with different strain measuring systems, i.e., since three specimens of each laminate were tested: the first one used strain gauges only, the second one used both systems and the third one used Aramis only. This procedure is done due to the fact that only strain gauges are a certified metrological equipment because it is the only method in which the stiffness of the structure is assured.

Once this kind of experiment is particularly susceptible to buckling, antibuckling rigs were utilised as is visible in figure 8.

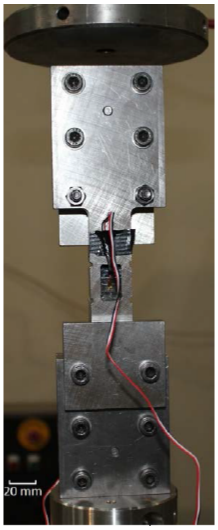

Figure 8: Photograph of the test set-up of a UC specimen equipped with an anti-buckling rig [11].

3.2.3 Experimental results for unnotched specimens

Once the experiments were performed, the ultimate load was recorded and the value obtained for each laminate can be analysed in table 4.

Table 4: Experimental values obtained for the unnotched specimens [26].

Lay-up	Specimen	$\bar{\boldsymbol{\sigma}}^{\infty}$ [MPa]
1	UT1	1022.1
	UT2	1043.5
	UT3	1094.7
1	UC1	538.9
	UC2	503.8
	OC3	573.5
2	UT1	944.4
	UT2	1017.2
	UT3	956.9
2	UC1	524.7
	UC2	482.3
	UC3	501.7

The mean of the values presented in the table above leads to the laminates' unnotched compressive and tensile strengths which are presented in the following table.

Table 5: Mean of the experimental values obtained for the unnotched specimens [26].

Lay-up	X_L^T [MPa]	X_L^C [MPa]
1	1053.5	538.7
2	972.8	502.9

3.3 Compact Tension and Compression

Compact Tension and Compression tests were performed so that the fracture toughness associated with longitudinal failure would be obtained for the T800/M21 composite, for lay-up 0.

The tests were not performed according to any standard because one does not yet exist. However, a procedure has been developed ([10],[27], [34], [29], [16], [21]) and a simple explanation of it will be presented in this chapter.

The material was loaded using the MTS-LoadCell-100 KN testing machine at a constant velocity of 2 mm/min in the direction of the **0°** laminates. The elastic properties of the laminate were then calculated by using ESAComp 3.5 [1].

In order to obtain strain values, the surface of the material was painted white with black dots as speckle pattern, which allows the use of Aramis DIC.

In this test, it is important to focus on the likelihood of buckling occurrence due to the high loads required to propagate the crack. In order to minimize its existence, steel anti-buckling rigs were introduced to the experiment [26].

3.3.1 Tension

The specimens used to perform the compact tension experiment can be seen in a simplified representation in figure 9, below, and their dimensions in table 6.

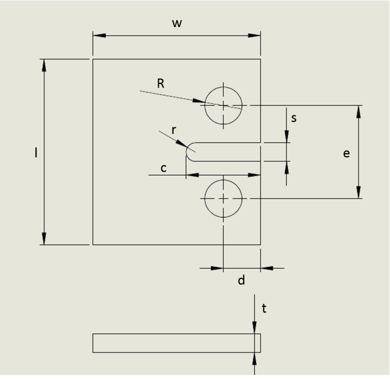

Figure 9: Geometric representation of the specimen for Compact Tension experiments.

Table 6: Dimensions of the Compact Tension specimens.

l	w	c	d	s	e	R	t
67 mm	67 mm	32 mm	10 mm	4 mm	30 mm	6.5 mm	4 mm

In these tests, an attainment of a smooth speckle pattern in the surface of the T800/M21 composite was difficult and so, the Aramis measurements were deemed invalid.

As an alternative, a ruler with real mm scale was attached to the surface of the specimen near the notch's edge where the opening of the crack occurs - see figure 10. Then, with the help of photographic evidence, the propagation of the crack is analysed.

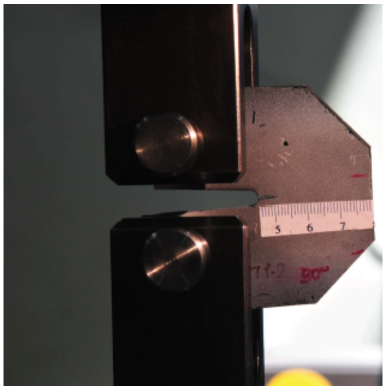

Figure 10: Photograph of the CT specimen equipped with a ruler [26].

Once the experiments were carried out, it was apparent that anti-buckling measures had to be taken. Cutting the free edges at a **45°** angle did not solve the problem and so, anti-buckling rigs were installed on the free surface of the specimens [26].

3.3.2 Compression

Here, the tests were made aiming the achievement of the value of fracture toughness associated with fibre kinking.

As a preventive measure, so there is no contact between the opposite sides of the notch, the geometry of the specimens utilised in this test is slightly different as the one of the compression specimens [26]. A bigger gap is drilled and the edge of the notch is differently filleted as well - see the figure below (figure 11).

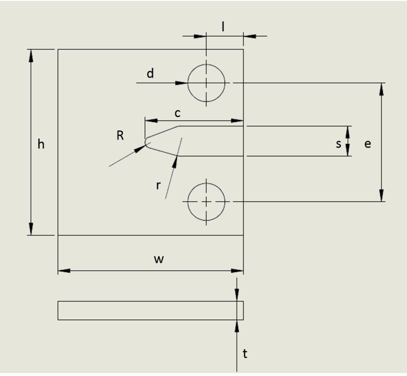

Figure 11: Geometric representation of the specimen for CC experiments.

Table 7: Dimensions of the Compact Compression specimens.

l	w	c	d	s	e	R	t
67 mm	67 mm	32 mm	10 mm	12 mm	48 mm	6.5 mm	4 mm

Note, however, that the stress intensity factor is not significantly affected by the geometry of the gap, as proven in [27].

3.3.3 Experimental results for Compact Tension and Compression specimens

Once the tests were concluded, the fracture toughness was calculated as a function of the crack length ($\boldsymbol{a}$) during propagation, defined according to the J-Integral Method, and knowing the applied load marked by the MTS-LoadCell [26].

$$\boldsymbol{G_{2\pm}} = \left(\frac{\boldsymbol{P^{\infty}}}{\boldsymbol{h}}\right)^{\mathbf{2}} \boldsymbol{f(a)}$$

Table 8: Experimental values obtained for the Compact Tension and Compression specimens [26].

Lay-up	Specimen	P^{∞} [N]	G_{2+} $[J/mm^2]$	G_{2-} $[J/mm^2]$
0	CT1	6890.6	100.5	
	CT2	-	-	
	CT3	-	-	
	CT4	6076.6	84.5	
0	CC1	-4743.5		89.5
	CC2	-4721.4		88.6
	CC3	-4383.4		76.4
	CC4	-4652.4		86.1

From the table above, one may reach the conclusion that the longitudinal compressive fracture toughness, $\boldsymbol{G_{2-}}$ for the $\mathbf{[90/0]_{8s}}$ laminate is $\mathbf{85.1}\boldsymbol{J/mm^2}$. The longitudinal tensile fracture toughness, $\boldsymbol{G_{2+}}$, on the other hand, may only be estimated as $\mathbf{92.5}\boldsymbol{J/mm^2}$ since two of the tension specimens buckled and just the initiation values of the laminate fracture toughness were used [26].

3.4 Center-Cracked

The experiment under review in this chapter has the purpose of measuring the fracture toughness of specimens with different notch dimensions. However, the basic geometry of the specimens is the same for all experiments and can be seen in figure 12.

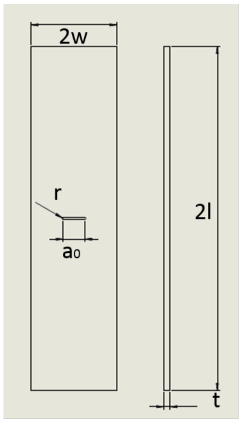

Figure 12: Geometric representation of the Center-Cracked specimen.

The metrological apparatus used to measure strain values were both strain gauges and the Aramis Digital Image Correlation system, and so, the specimens were prepared accordingly.

In order to make the crack in the center of the specimen, firstly a hole is drilled with a 1 mm drill bit which does not lead to sharp crack tips; This simplification can be made since the specimen fails when the crack has already propagated until its critical length, which means that the crack tip is sharp. Also it has been shown that the use of a drill and a thin saw is virtually the same [27].

3.4.1 Tensile Tests

The experiments performed for tensile tests used T800/M21 (lay-up 1 and 2) and were done according to ASTM Standard D3039 [7] and again, using the MTS 810 testing machine and the 100 KN LoadCell, at a steady velocity of 2 mm/min.

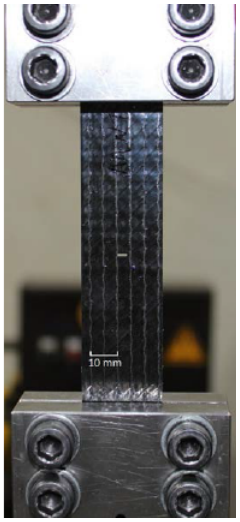

Figure 13: Photograph of the test set-up for the Center-Cracked tension specimens. [11]

In order to comprehend the importance of the effect of the size of the notch, both laminates were tested on specimens of different dimensions that can be seen in table 5 [26].

Table 9: Dimensions of the Center-Cracked tension specimens.

Lay-up	Specimen	2l [mm]	2w [mm]	t [mm]	$\boldsymbol{a_0}$ [mm]
1 and 2	1	250	12	3	2.2
	2	250	16	3	3.2
	3	250	22	3	4.4
	4	250	30	3	3

3.4.2 Compressive Tests

Once again, the compressive experiments were performed according to the ASTM Standard, D3410 specifically [4]. At a constant speed of 2 mm/min, lay-ups 1 and 2 were tested with the MTS 810 testing machine and the 100 KN LoadCell in order to obtain the compressive fracture toughness.

The specimens used had different dimensions (see table 10) so as to determine the dependence of the material on size, in its compressive response.

Table 10: Dimensions of the Center-Cracked compression specimens.

Lay-up	Specimen	2l [mm]	2w [mm]	t [mm]	a_0 [mm]
1 and 2	1	305	12	3	2.4
	2	305	16	3	3.2
	3	305	22	3	4.4
	4	305	30	3	3

Once again, in order to prevent buckling occurrence , anti-buckling rigs were used in the tests as is apparent in figure 14.

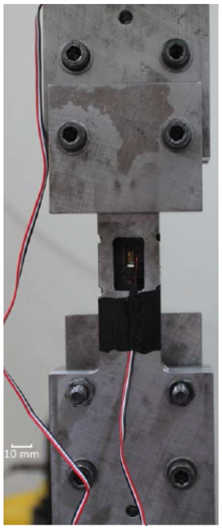

Figure 14: Photograph of the set-up for the Center-Cracked compressive tests. [11]

3.4.3 Experimental results for the Centre-Cracked specimens

Since the experiment under review was performed to obtain the fracture toughness of the two different laminates, the Soutis-Fleck model [37] was used as so:

$$G_{2\pm} = \frac{K_c^2}{E^*}$$

$$E^* = \frac{\sqrt{2E_Y E_X}}{\sqrt{\sqrt{\frac{E_Y}{E_X}} + \frac{E_Y}{2G_{XY}} - \nu_{YX}}}$$

$$\boldsymbol{K_c = Y\bar{\sigma}^{\infty}\sqrt{\pi a}}$$

Where $\boldsymbol{\bar{\sigma}^{\infty}}$ is the remote stress at failure measured in the tests, Y is the finite width correction factor, function of the $\boldsymbol{w}$ and $\boldsymbol{a_0}$ present in figure 12. The elastic properties enunciated were calculated using lamination theory with the axis x aligned with the loading direction [26].

Using the equations enumerated above and the elastic properties of the laminate, the fracture toughness of the laminates can be calculated and they are presented in table 11.

Table 11: Experimental values obtained for the Center-Cracked specimens [26].

Lay-up	Specimen	$\boldsymbol{\sigma^{\infty}}$ [MPa]	$\boldsymbol{G_{2+}}$ $\boldsymbol{[KJ/m^2]}$	$\boldsymbol{G_{2-}}$ $\boldsymbol{[KJ/m^2]}$
1	CCT1	601.4	21.6	
	CCT2	545.2	23.7	
	CCT3	518.6	29.5	
	CCT4	649.8	31.3	
1	CCC1	-269.4		4.5
	CCC2	-250.8		5.2
	CCC3	-253.0		7.3
	CCC4	-366.9		10.0
2	CCT1	651.4	25.1	
	CCT2	612.9	29.8	
	CCT3	541.5	33.1	
	CCT4	665.3	34.3	
2	CCC1	-307.8		5.6
	CCC2	-349.2		9.6
	CCC3	-298.8		9.7
	CCC4	-387.4		11.1

3.5 Double-Edge Cracked

Even tough Compact Compression tests can be used to reliably measure the value of the fracture toughness, they do not allow the acquiring of the relation that it has with the increasing crack length, in other words, it does not give the crack resistance curve. It has also been shown that, with Compact Tension/Compression specimens, it is not possible to measure the fracture toughness of modern resin systems which lead to higher values of fracture toughness [26]. With this in mind, Double-Edge Cracked specimens were used to perform tensile and compressive experiments. Both T800/M21 and IM7/8552 were utilised in this experiment with the lay-ups 0 and 3.

So as to follow the propagation of the crack, all the specimens were painted white with a speckle, permitting the use of the Digital Image Correlation (DIC) system.

3.5.1 Tensile Tests

Six specimens with different widths and crack lengths (see figure 15 and table 12) were produced with the support of a CNC machine equipped with a 1 mm drill bit which does not lead to sharp crack tips; however, as mentioned before, it has been proven that the fracture toughness obtained with a crack machined using a drill bit and using a thin saw is virtually the same [16].

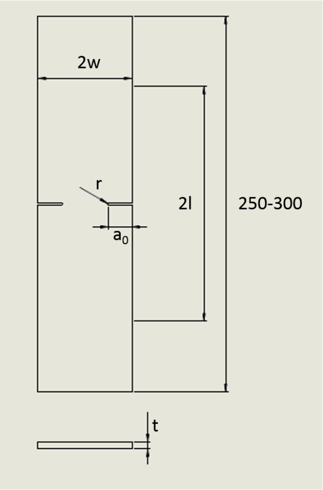

Figure 15: Geometric representation of the Double-Edge Cracked specimen used for tensile tests.

Table 12: Dimensions of the Double-Edge Cracked tension specimens.

Lay-up	Specimen	2w [mm]	a_0 [mm]	t [mm]
0	1	10	3	2
	2	15	4.5	2
	3	25	7.5	2
	4	35	10.5	2
3	5	15	4.5	2
	6	20	6	2
	7	25	7.5	2
	8	30	9	2

The material was then tested with three exemplars of each size at a constant speed of 1 mm/min using an Instron 4208 testing machine equipped with a 100kN load cell [19].

3.5.2 Compressive Tests

These experiments were performed with an Instron 4208 universal testing machine at a constant displacement rate of 0.1 mm/min. Once again, the loads were measured using a 100 KN LoadCell but in this particular experiment, only IM7-8552 was tested with a $[\mathbf{90/0}]_{\mathbf{8s}}$ lay-up (lay-up 3).

The geometry of the specimens is defined according to figure 16 and their dimensions can be seen in table 13, being that the notches were produced using a vertical mill with a 1 mm diameter drill bit and six different sizes of proportional specimens were produced and three of each tested [22]. The initial crack length (a_0) is defined as half the characteristic length for all specimens.

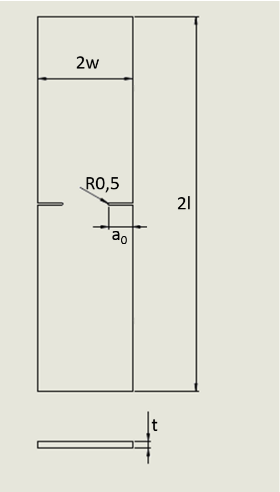

Figure 16: Geometric representation of the Double-Edge Cracked specimen used for compressive tests.

As is visible in the figure above, the crack faces are separated by a distance of 1 mm in order to ensure that there is no contact between them during compression.

Table 13: Dimensions of the Double-Edge Cracked compression specimens.

Lay-up	Specimen	2w [mm]	2l [mm]	a_0 [mm]	t [mm]
3	1	10	15	2.5	4
	2	15	22.5	3.75	4
	3	20	30	5	4
	4	25	37.5	6.25	4
	5	30	45	7.5	4
	6	35	52.5	8.75	4

Since compressive tests in the longer specimens may result in buckling occurrence, these specimens were equipped with strain gauges from Vishay Micro-Measurement and the Spider data acquisition system used to record its signal.

The specimens were equipped with tungsten-carbide inserts as to prevent friction and deformation [22].

3.5.3 Experimental results for the Double-Edge Cracked specimens

The experimental results obtained for all of the Double-Edge Cracked specimens can be analysed in table 14, where the ultimate stress and standard deviation of the tests is presented.

Table 14: Experimental values for the DEC specimens [22], [19].

Lay-up	Specimen	$\bar{\sigma}^{\infty}$ [MPa]	STDV [MPa]
0	DET1	484.0	20.0
	DET2	426.0	22.0
	DET3	380.0	35.0
	DET4	299.0	19.0
3	DET5	309.0	9.0
	DET6	289.0	16.0
	DET7	269.0	11.0
	DET8	256.0	10.0
3	DEC1	284.8	1.4
	DEC2	258.0	0.4
	DEC3	218.0	0.5
	DEC4	226.2	0.2
	DEC5	205.9	0.1
	DEC6	183.1	0.1

3.6 Open Hole

Different experiments were performed with Open Hole specimens. In [26], the T800/M21 composite was used, in both lay-ups 1 and 2, to manufacture 3 different specimen dimensions with a growing hole diameter of 3 mm up to 7 mm and a constant ratio of $\boldsymbol{\frac{w}{d} = 4}$.

In [18], however, as to validate the utility of the Continuum Damage Model in strength and size effects prediction, the IM7/8552 composite with a lay-up of $\boldsymbol{[90/0/\pm 45]_{3s}}$ (lay-up 5) is tested in tension tests with specimens that have a hole diameter of from 2 mm to 10 mm and a constant ratio of $\boldsymbol{\frac{w}{d} = 6}$.

The basic configuration and general dimension of all the specimens manufactured can be seen in figure 17.

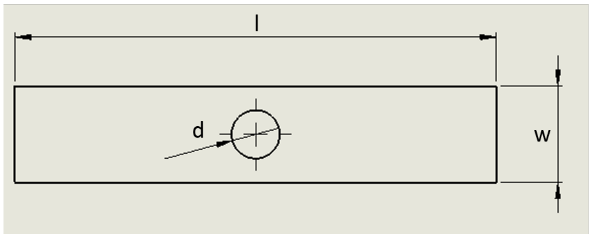

Figure 17: Geometric representation of the specimen for Open Hole strength experiments.

Again, in these experiments, an MTS-100 KN LoadCell was used at a constant velocity of 2 mm/min and in order to record strain values, both strain gauges and Aramis were used and their results compared.

3.6.1 Tensile Tests

The procedures used to perform the tensile tests follow the ASTM Standard D5766 [5] and lay-ups 1, 2 and 5 were tested, as mentioned before.

The strain values were obtained using strain gauges from Vishay with strategic placings [18] - see figure 18, but then, for matters of validation of this system, Aramis was also used.

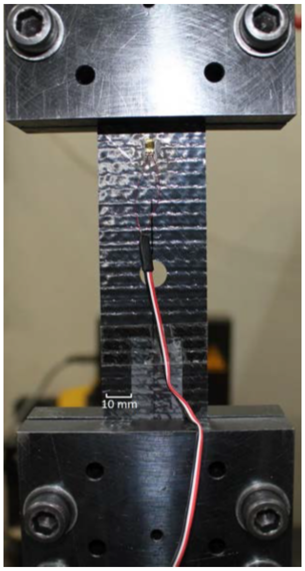

Figure 18: Photograph of the test set-up for the OHT specimens [11].

Both lay-ups of the T800/M21 composite were manufactured with the same geometry and, for each stacking sequence, 3 specimens of each geometry were tested. The IM7/8552's lay-up, on the other hand, was tested with 5 different specimens of each geometry, that is itself different from the geometry of the T800 - (see table 15).

Table 15: Dimensions of the Open Hole Tension specimens.

Lay-up	Specimen	l [mm]	w [mm]	t [mm]	d [mm]
1 and 2	1	250	12	3	3
	2	250	20	3	5
	3	250	28	3	7
5	4	200-300	12	3	2
	5	200-300	24	3	4
	6	200-300	36	3	6
	7	200-300	48	3	8
	8	200-300	60	3	10

The DIC system was also used to identify the first ply failure load and the sequence of failure mechanisms on the surface of the **90°** ply [26] for later extraction of ply properties.

3.6.2 Compressive Tests

Since this kind of compressive tests is susceptible to buckling, anti-buckling rigs were again utilised when testing the specimens [26] - see figure 19.

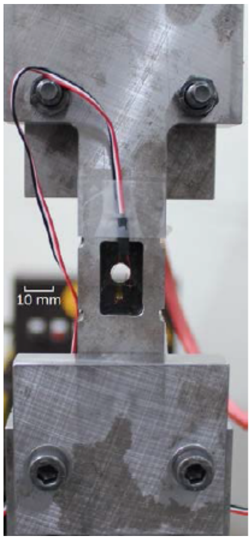

Figure 19: Photograph of the test set-up for the OHC specimens. [11]

The standard in which these experiments were based is the ASTM Standard D6484 [8] and the dimensions of the specimens manufactured is given in table 16.

Table 16: Dimensions of the Open Hole Compression specimens.

Lay-up	Specimen	l [mm]	w [mm]	t [mm]	d [mm]
1 and 2	1	305	12	3	3
	2	305	20	3	5
	3	305	28	3	7
5	4	300	12	3	2
	5	300	18	3	3
	6	300	24	3	4
	7	300	30	3	5

3.6.3 Experimental results for the Open Hole specimens

For each test, the failure load was registered which allows the definition of the remote failure stress using the expression $\bar{\boldsymbol{\sigma}}^{\boldsymbol{\infty}} = \frac{\bar{\boldsymbol{P}}}{\boldsymbol{wt}}$, being $\bar{\boldsymbol{P}}$ the failure load measured in the tests and $\boldsymbol{t}$ and $\boldsymbol{w}$ the measured thickness and width of the specimens, respectively.

Since different specimens of each dimension were tested, the mean values of the remote failure and the standard deviation are presented in table 17 for the tensile and compressive tests of all laminates.

Table 17: Experimental Values for the OH specimens [18].

Lay-up	Specimen	$\bar{\sigma}^{\infty}$ [MPa]	STDV [MPa]
1	OHT1	560	15.5
	OHT2	534	11.9
	OHT3	500	16.9
1	OHC1	334.5	39.4
	OHC2	372.9	13.6
	OHC3	365.2	5.3
2	OHT1	565	21.1
	OHT2	536	11.6
	OHT3	258.8	5.3
2	OHC1	325.4	19.6
	OHC2	299.7	15.1
	OHC3	283.4	12.6
3	OHT12	555,7	15.3
	OHT24	480,6	21.4
	OHT36	438,7	25.3
	OHT48	375,7	15.1
	OHT60	373,7	14.1
3	OHC12	383.1	-
	OHC18	372.9	-
	OHC24	365.2	-
	OHC30	353.7	-

3.7 Bolted joint

When subjected to bolted joint tests, composites can fail in various manners, the most common being net-tension, bearing and shear-out, represented in figure 20.

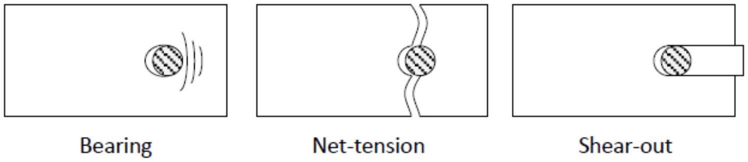

Figure 20: Simplified representation of common joint failure modes [11].

The basic geometry and dimensions of the type of specimens experimented on in the bearing tests can be seen in figure 21.

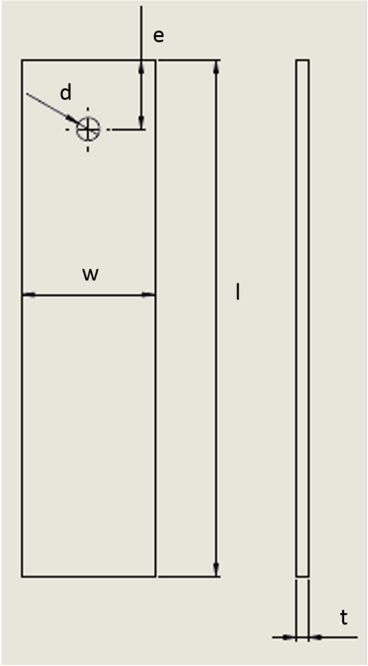

Figure 21: Simplified representation of the typical geometry of a bearing specimen and its basic dimensions [6].

Depending on the type of mechanical element used, a pin or a screw fastened with a bolt and a washer, the bearing test is called either pin- or bolt-bearing. Both the tests were performed. Another form of distinguishing bearing tests is by the amount of holes drilled in the specimens, either one or two, making the test single- or double-shear lap joints, respectively. The following sections are divided according to both these criteria.

3.7.1 Single-shear lap joints

3.7.1.1 Bolt-Bearing

The purpose of bolt-bearing tests is evaluating the mechanical behaviour of the thin-ply laminates when subjected to local compressive efforts, which typically occurs with mechanically fastened joints.

The type of failure mode described in this subsection is a non-catastrophic one that results from a progressive accumulation of damage that subsequently results in a permanent deformation of the hole in compression. The bolt-bearing tests were performed according to ASTM Standard D5961 [6].

In order to perform the tests, a M6 bolt is used with an applied torque of 2.2 N.m, and then, under displacement control, in a servo-hydraulic MTS 810 testing machine, one specimen per geometry was instrumented equipped with a strain gauge in the longitudinal direction.

In order to avoid sliding between the specimens and the loading system, sandpaper strips (IMPERIAL CRD 40) were placed in the grip that supports the end opposite to the bearing region and a guiding pin was placed to ensure the alignment of the longitudinal axis. Test set-up can be seen in the figure below.

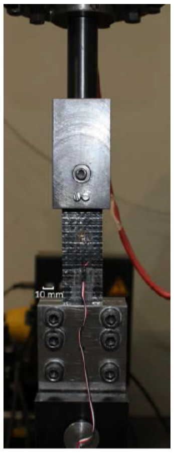

Figure 22: Photograph of the set-up for the bolted bearing tests [11].

The dimensions of the specimens used in the single bolt-bearing tests can be seen in table 18, keeping in mind that five specimens of each dimension were tested. The $\boldsymbol{d_W}$ that appears in the table represents the diameter of the washers used.

Table 18: Dimensions of the single bolt-bearing specimens.

Lay-up	Specimen	2l [mm]	2w [mm]	e [mm]	t [mm]	d [mm]	$\boldsymbol{d_w}$ [mm]
3	1	135	36	18	3	6	12
	2	135	48	24	3	8	13
	3	135	60	30	3	10	14.5

3.7.1.2 Pin-Bearing

In this test, again, the purpose is to study how the material reacts to a connection, now with a pin. The main difference to shed light on is the fact that here no clamping pressure is applied.

The same ASTM Standard is used for these tests, the D5961 one [6], just as the same procedure is used to avoid sliding.

The specimens used in the single pin-bearing tests had a basic geometry as shown in figure 21 and their dimensions can be seen in table 19, keeping in mind, once again, that five specimens of each dimension were tested.

Table 19: Dimensions of the single pin-bearing specimens.

Lay-up	Specimen	2l [mm]	2w [mm]	e [mm]	t [mm]	d [mm]
3	1	135	36	18	3	6
	2	135	48	24	3	8
	3	135	60	30	3	10

3.7.2 Double-shear lap joints

Even though the specimen used in the double-shear tests is similar to the single-shear tests, it is important to note that the distance between the drilled holes is defined in the D5961 ASTM Standard [6], and so, a representation of the specimens' geometry is presented in figure 23 .

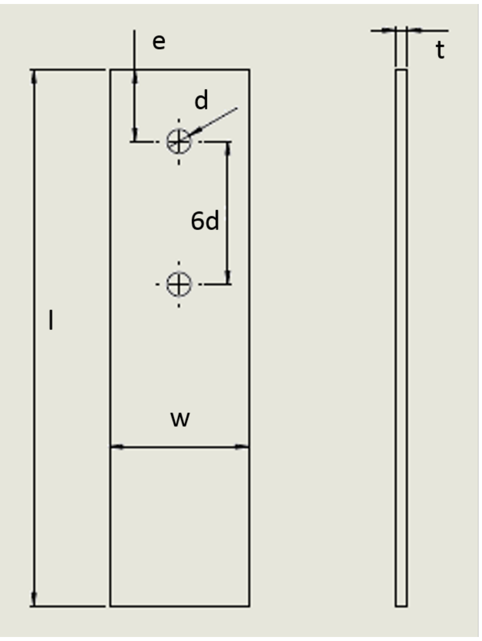

Figure 23: Simplified representation of the typical geometry of a double-shear lap joints specimen and its basic dimensions [6].

3.7.2.1 Bolt-Bearing

The M6 bolt is used again to join the specimens with a clamping pressure of 2.2 N.m, and then, under displacement control, in a servo-hydraulic MTS 810 testing machine, one specimen per geometry was tested. Sliding was once more prevented with sandpaper.

The dimensions of the specimens used is represented in table 20.

Table 20: Dimensions of the double bolt-bearing specimens.

Lay-up	Specimen	2l [mm]	2w [mm]	e [mm]	t [mm]	d [mm]
3	1	135	12	24	3	6
	2	135	36	9	3	6
	3	135	42	21	3	7

3.7.2.2 Pin-Bearing

Using the same methodology, the double-shear pinned specimens were tested with the geometry presented in table 21.

Table 21: Dimensions of the double pin-bearing specimens.

Lay-up	Specimen	2l [mm]	2w [mm]	e [mm]	t [mm]	d [mm]
3	1	135	12	24	3	6
	2	135	36	9	3	6
	3	135	42	21	3	7

3.7.3 Experimental results for bolted/pinned joint specimens

Since the maximum load and the laminates failure mode and its location were recorded for each specimen after the tests, the results for the single-bearing bolted/pinned (SBB/P) and the double-bearing bolted/pinned (DBB/P) specimens may be analysed in table 22.

Table 22: Experimental results for the bearing specimens [17].

Specimen	$\boldsymbol{\sigma^b}$ [MPa]	STDV [MPa]	failure mode
SBP1	697.0	17.5	
SBP2	686.0	47.3	
SBP3	724.5	24.2	
SBB1	747.1	5.9	
SBB2	740.4	23.6	
SBB3	701.9	23.6	
DBP1	460.5	-	tension
DBP2	699.4	-	bearing+shear
DBP3	706.3	-	bearing
DBB1	526.5	-	tension
DBB2	701.8	-	bearing+shear
DBB3	695.2	-	bearing

3.8 Experimental Properties of the Material

Using the plain strength tests, the remote stress at failure can be measured which allows for the definition of the unnotched strengths ($\boldsymbol{X^L_{T/C}}$), empirical data important for the numerical models. Following the same reasoning, $\boldsymbol{G_{2+}}$ and $\boldsymbol{G_6}$ that correspond to the fracture toughness of a transverse crack in mode I and II, respectively, can be measured using the Double Cantilever Beam (DCB) test [2] and the Four-Point End Notched Flexure (4-ENF) test specimen [32], respectively.

The mode I component of the fracture toughness for a longitudinal crack - $\boldsymbol{G_{1+}}$ - does not have a standard test method to measure its value. In [31], the Compact Tension (CT) test specimen proposed by [33] is suggested.

For the attainment of $\boldsymbol{G_{1-}}$, in [12] it is proposed the following expression to evaluate the energy dissipated per unit area in a kink band: $\boldsymbol{G_{1-} = \frac{w}{s} G_6}$; where $\boldsymbol{w}$ is the kink band thickness and $\boldsymbol{s}$ is the distance between two matrix cracks [31].

The definition of the materials used in the experimental tests can at this point be completed, leading to table 23 that presents the properties for the IM7/8552 material used in the simulations.

Table 23: Material properties for IM7/8552 obtained experimentally[18].

	IM7/8552
	lay-up 3
$\boldsymbol{X_T^L}$	$\boldsymbol{845.1MPa}$
$\boldsymbol{X_C^L}$	$\boldsymbol{532.6MPa}$
$\boldsymbol{K_{Ic}}$	$\boldsymbol{48.0MPa\sqrt{m}}$
$\boldsymbol{G_{2+}}$	$\boldsymbol{0.2774KJ/m^2}$
$\boldsymbol{G_6}$	$\boldsymbol{0.7879KJ/m^2}$
$\boldsymbol{G_{1+}}$	$\boldsymbol{81.5KJ/m^2}$
$\boldsymbol{G_{1-}}$	$\boldsymbol{106.3KJ/m^2}$

Because the T800/M21 was not used for numerical analysis, there was no preoccupation in attaining its mechanical properties at the same level of detail as the IM7. However, for both lay-ups 1 and 2, the unnotched strength and stress intensity factor were obtained and are presented in table 24.

Table 24: Material properties for T800/M21 obtained experimentally.

	T800/M21	
	lay-up 1	lay-up 2
$\boldsymbol{X_T^L}$	$\boldsymbol{1053.5MPa}$	$\boldsymbol{972.8MPa\sqrt{m}}$
$\boldsymbol{X_C^L}$	$\boldsymbol{539.0MPa}$	$\boldsymbol{5033.0MPa\sqrt{m}}$
$\boldsymbol{K_{Ic}}$	$\boldsymbol{56.7MPa\sqrt{m}}$	$\boldsymbol{56.7MPa\sqrt{m}}$

4 Prediction of damage propagation and fracture of the IM7/8552

To perform the numerical analysis of the specimens using IM7/8552 CFRP in a $\mathbf{[90, 0, \pm 45]_{3s}}$ lay-up, Abaqus was used in the explicit mode to implement user subroutines.

In this chapter, the implementation of the models and criteria used in the routines will be described bearing in mind that this method was used so as to overcome the restrictive input methods sometimes provided by Abaqus's capabilities [25].

In order to test the various routines developed, their submission was made in the Avalanche Linux cluster with a 2xIntel E5-2450 CPU consisting of a total of 16 CPU cores, at FEUP.

4.1 Implementation

Since both non-linear behaviour and contact between plies are under review, the use of Abaqus/Explicit is justified for the analysis of the loading of the increasingly complex specimens.

The following chapter is divided in 3 different parts that correlate with the main subjects dealt with in the routines: the mesh, the surface interaction and the models and criteria implemented in the routines.

Quasi-static simulations are performed, which means that the velocity defined is low and so the kinetic energy is very small relatively to the peak internal energy. Therefore, a balance must be achieved between the quality of the results (low relative errors) and the time spent running the routines. To do so, there was the preoccupation of analysing mass scaling and increasing and decreasing the amount of non-physical mass added in order to obtain a balance between quality and time management.

4.1.1 Mesh

To develop the mesh, an analysis of the different forms of constructing it was performed. A non-structured mesh could be used as described in

[26], for its simplicity, and, on the other hand, a structured mesh could be implemented as well in the expectation of better results.

A structured mesh has the advantage of initially allowing the opening of the crack according to fibre direction just like it happens in the experimental tests, while a simple a non-structured mesh does not allow for that phenomenon to be properly represented (see figure below).

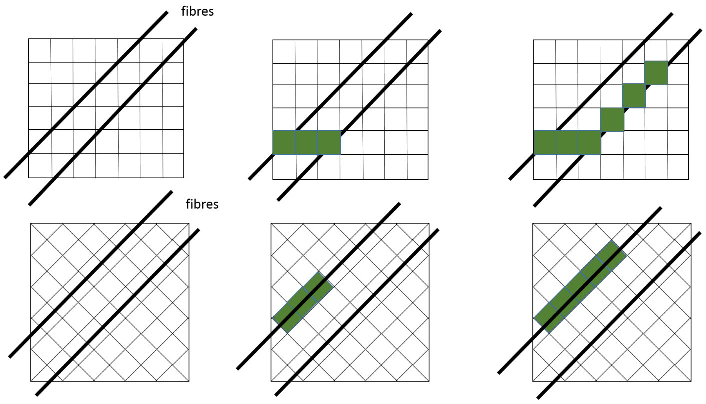

Figure 24: Scheme representing crack propagation in non-structured and structured mesh, respectively.

With that in mind, a structured mesh was developed in the work performed by Hilal Erçin [26] with the help of input files for Abaqus/Explicit and that was the one used in the simulations.

The type of element used was a 3D hexahedral element with 8 nodes, C3D8R, and a critical length for it had to be defined in the VUMAT for the constitutive model not to lead to a local snap-back in the stress - strain relation [31] - see Chapter 2. The critical dimension is then defined according to the following expression:

$$\boldsymbol{l^*_{max} = \frac{2E_M G_M}{X_M^2}}$$

If this critical dimension of the element is exceeded, the routine is implemented so as to reduce the strength $\boldsymbol{X_M}$.

Exceptionally, in the $\pm\mathbf{45}$ plies of the Open Hole specimens, some 6-node linear triangular prism elements had to be used so as to accommodate the hole, despite their poor convergence rate. In this case, the first order C3D6 element was chosen.

Since a non-linear and catastrophic analyses was performed, there was the concern of activating the hourglass control which prevents an excessive distortion due to the elements instability that results from reduced integration [25].

4.1.2 Cohesive behaviour

To define the relation between the lamina, cohesive surfaces where defined in user subroutines so as to best represent delamination. Using the surfaces allows for the specification of generalised traction-separation behaviour between two adjacent surfaces. It is easier to define in multi-directional laminates than cohesive elements and allows the simulation of a wider range of cohesive interactions [42].

A cohesive surface relates the loading transmitted over the surface to the separation between the surfaces not affecting the stiffness of the material. Furthermore, during damage evolution, the ability to transmit tractions over the cohesive surface is affected while the rest of the material remains elastic. Delamination thus progresses solely based on the strength degradation in the cohesive surfaces and the interaction with the elastic regions of the material [38].

The routines were submitted at first with Abaqus' surface interaction defined. However, as can be seen in [35] and [36], the software has an implementation error related to the B-K criterion [13] that over-predicts the analytical results by as much as $\mathbf{35\%}$ [36]. However, when the B-K criterion is supplied in a user defined tabular form, the results correlate much better with the analytical solution [36]. That said, in an attempt to correct the error in question, a user surface interaction was implemented in the code specifying the $\boldsymbol{G_c}$ in tabular form as a function of the mode mixity ratio [36] - see Appendix A.

In a more technical note, an uncoupled traction-separation behaviour is defined, which means that each traction component depends only on its conjugate separation, and the stiffness coefficients ($\boldsymbol{K_{nn}}$, $\boldsymbol{K_{ss}}$ and $\boldsymbol{K_{tt}}$) are supplied with this in mind, satisfying the requirements for the equation below.

$$\begin{Bmatrix} \boldsymbol{t_n} \\ \boldsymbol{t_s} \\ \boldsymbol{t_t} \end{Bmatrix} = \begin{bmatrix} \boldsymbol{K_{nn}} & \boldsymbol{K_{sn}} & \boldsymbol{K_{tn}} \\ \boldsymbol{K_{ns}} & \boldsymbol{K_{ss}} & \boldsymbol{K_{ts}} \\ \boldsymbol{K_{nt}} & \boldsymbol{K_{st}} & \boldsymbol{K_{tt}} \end{bmatrix} \begin{Bmatrix} \boldsymbol{\delta_n} \\ \boldsymbol{\delta_s} \\ \boldsymbol{\delta_t} \end{Bmatrix}$$

With $\boldsymbol{t}$ being the nominal traction stress vector, $\boldsymbol{\delta}$ the separations and $\boldsymbol{K}$ the stiffness parameter. The latter assures a stiff connection between two layers before delamination initiates and it should be large enough to provide a reasonable stiffness but small enough to avoid numerical problems [39], the values chosen are between $\mathbf{10^5}$ and $\mathbf{10^6}$. The rest of the stiffness parameters are added by Abaqus by default.

When it comes to the beginning of degradation of the cohesive response, the chosen criterion is the Maximum Stress Criterion in which damage initiates once the maximum contact stress ratio satisfies the damage initiation criteria presented below [25].

$$\boldsymbol{MAX} \left\{ \frac{\langle \boldsymbol{t_n} \rangle}{\boldsymbol{t_n^0}}, \frac{\boldsymbol{t_s}}{\boldsymbol{t_s^0}}, \frac{\boldsymbol{t_t}}{\boldsymbol{t_t^0}} \right\} = \mathbf{1}$$

After damage initiation, the rate at which the cohesive stiffness is degraded must also be defined, i.e., the damage evolution criterion must also be chosen. For the reasons previously presented, an energy based damage evolution criterion was defined in tabular form - see Appendix A. This type of evolution is based on the definition of the fracture energy dependant on the mode mix and so, the variable is specified as a property of the cohesive interaction.

4.1.3 Models and criteria implemented

The models and criteria implemented are mainly specified in the VUMAT which is divided as to simulate two different constitutive behaviours: interlaminar fracture (delamination) and intralaminar fracture.

The simulation of **interlaminar fracture** is developed using user defined surface interactions, which were mentioned in the chapter above.

The **intralaminar fracture** is simulated using a new 3D invariant-based failure criteria [14] making a distinction between longitudinal and transverse failure, since the matrix-dominated failure (transverse failure) allows for the use of the Smeared Crack Model while the fibre-dominated one (longitudinal failure) does not. This is due to the fact that this failure mechanism consists of the fracture of the reinforcing fibres and matrix but also of fibre-matrix debonding and there are not yet well-established methods of characterization of the fracture toughness for fibre dominated failure mechanisms under general loading conditions.

Therefore, to represent longitudinal failure mechanisms, a modification of the Continuum Damage Model developed in[30] taking into account the *in-situ* strengths, i.e., the increase of the shear strength of a ply when embedded in a multi-directional laminate, as seen in 2.2, is used.

4.1.3.1 Failure Criteria

Analysing the failure criteria for **longitudinal fracture**, one must note that tensile and compressive failure are differently predicted.

Tensile fracture in the fibre direction is predicted using the non-interacting maximum allowable strain criterion as defined in section 2.2.2 and remembered below:

$$\boldsymbol{\phi_{1-} = \frac{\varepsilon_{11}}{\varepsilon_1^T}}$$

When it comes to longitudinal compressive failure, the mechanisms in play are more complex and therefore, so is the criterion implemented. As developed in section 2.2.2, the 3D kinking model based on the invariant failure criteria [14] formulated for transverse fracture, can be modified to consider the misalignment angle, allowing for the prediction of failure that occurs due to the presence of local micro-structural defects that trigger a kink band. The misalignment angle is calculated considering that $\boldsymbol{\phi_0 = 0}$.

Transverse failure does not require any alterations of the criteria and so the 3D invariant criteria is applied directly as developed in [14] and presented in section 2.2.1.

4.1.3.2 Damage Law

4.1.3.2.1 Longitudinal Failure

This type of failure mechanism has a damage evolution defined according to the Continuum Damage Model developed in [30] and presented in section 2.1 which is formulated defining the complementary free energy as a function of damage variables.

In order to track whether the kind of damage mechanisms in action is due to compression or tension, the model uses the damage mode, $\boldsymbol{d_1}$:

$$\boldsymbol{d_1 = d_{1+}\frac{\langle \sigma_{11} \rangle}{|\sigma_{11}|} + d_{1-}\frac{\langle -\sigma_{11} \rangle}{|\sigma_{11}|}}$$

To determine if damage has initiated, $\boldsymbol{F_{1+}}$ and $\boldsymbol{F_{1-}}$ are analysed and if it has, damage evolution is defined by the *Kuhn-Tucker* conditions:

$$\boldsymbol{r_N \geqslant 0; \quad F_N \leqslant 0; \quad r_N F_N = 0}$$

Meaning that while $\boldsymbol{F_N}$ is negative, the material has an elastic behaviour but when it reaches 0, there is damage evolution.

4.1.3.2.2 Transverse Failure

To implement the damage model, the Smeared Crack Model is used as described in 2.2.1. In sum, the model considers the projection of the tractions acting on the fracture plane onto the crack frame and the displacement jumps. The tractions acting on the fracture plane are defined as:

$$\boldsymbol{t_i^{cr} = \left(\frac{1-d}{d}\right)\frac{\omega_i^{cr}}{\omega_i^{m}}\bar{t}_i^{cr} - \delta_{i2}\frac{\langle -\omega_2^{cr} \rangle}{|\omega_2^{cr}|}\left[\left(\frac{1-d}{d}\right)\frac{\omega_i^{cr}}{\omega_f^{m}}\bar{t}_i^{cr} - E_2(\varepsilon_{22}^{cr} - \varepsilon_{c22}^{cr})\right]}$$

For the mixed-mode interlaminar fracture toughness to be predicted, the B-K criterion is used and it requires material properties that must be input such as the $\boldsymbol{\eta}$ parameter, that, for the material in question, IM7/8552, is 1.634.

The latest version of the VUMAT uses a backtracking scheme that complements the Newton-Raphson's method and leads to the faster reduction of the step in an attempt to minimize the number of iterations.

4.2 Comparison between experimental and numerical results

Once the routines were submitted, as a form of validation, the values obtained were compared to the experimental ones previously presented in chapter 3. In order to do so, the ultimate stress was calculated for the simulations and then the relative error was obtained for both Unnotched and Open Hole specimens.

In this section, the results for the plain strength and the OH specimens will be presented and analysed in two different subsections. The charts provided by Abaqus that display the raw data obtained for all specimens can be seen in Appendix B.

4.2.1 Unnotched specimens

Although the type of specimen under analysis is the simplest in terms of physical construction, it is one of the trickiest to simulate failure due to the non-existence of a crack to define were the fracture initiates. In another note, it is also important to ensure that there is no free edge effect. Free-edge damage is typically initiated as a result of the differences in the Poisson's ratio of adjacent lamina [41] and to prevent it, the specimen has to have sufficient width. This effect may cause failure of the material, beginning at the edges, with failure load values much lower than predicted.

By the first attempt it was clear that the specimens were not failing in a satisfactory manner, leading to high relative errors. That was happening due to the lack of crack initiation and immediate delamination and deformation until destruction, leading to a process with very high kinetic energy.

In order to get better results, the type of loading was changed from displacement control to velocity, defined by amplitude in a smooth step. By doing so, a time parameter also had to be defined and the value chosen was 0.0012. Mass scaling was also diminished from $\mathbf{10^{-6}}$ to $\mathbf{10^{-7}}$, increasing computing time (about an hour of walltime) but improving the results.

Since there is no stress concentration in the specimens and the strength field is uniform, there is no need to test different geometries of specimens and so, only a specimen of 12 mm in width and 3 mm thick is tested in both compressive and tensile simulations.

4.2.1.1 Compression

The virtual specimen had a structured mesh (see figure 25) and was simulated as a whole. That said, once the ultimate load value was obtained, the ultimate stress was easily calculated by dividing the load by the specimen's section area, which led to the results presented in table 25.

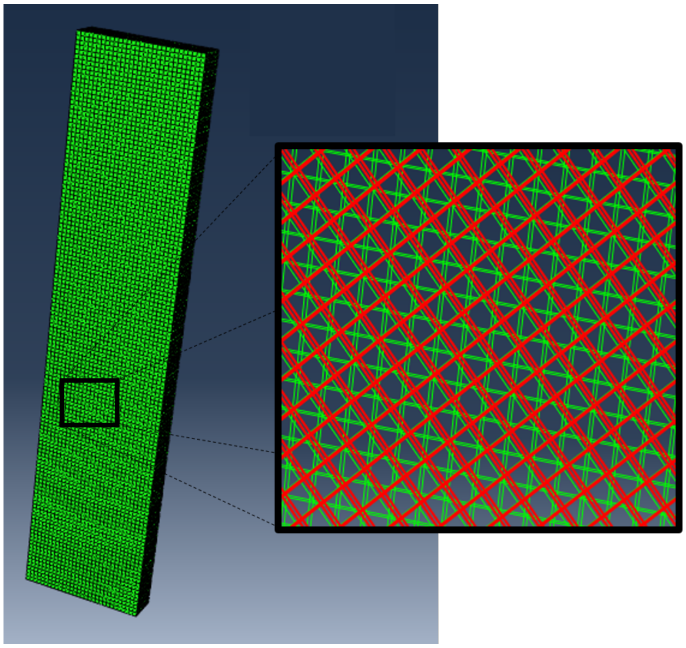

Figure 25: Virtual Unnotched Compression specimen and detail of the structured mesh.

Table 25: Analytical results for the Unnotched Compression specimen.

Specimen	$\boldsymbol{P^{\infty}}$ [N]	$\boldsymbol{w}$ [mm]	$\boldsymbol{t}$ [mm]	$\boldsymbol{\sigma_{num}}$ [MPa]
UC	19457.3	12	3	540.5

After simulating the compressive test, the specimen failed near the bottom as represented in figure 26.

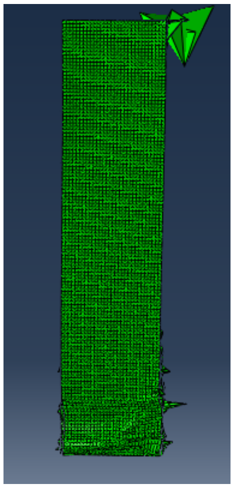

Figure 26: Virtual Unnotched Compression specimen after failure.

It is evident from the figure above that there was excessive distortion of elements in the top of the specimen; however, their placement does not impede the correct simulation of the compressive test.

4.2.1.2 Tension

A similar specimen as the one presented in figure 25 was used for the tensile numerical tests. The results of the simulation can be analysed in table 26 and the specimen after destruction can be seen in figure 27.

Table 26: Analytical results for the Unnotched Tension specimen.

Specimen	$\boldsymbol{P^{\infty}}$ [N]	$\boldsymbol{w}$ [mm]	$\boldsymbol{t}$ [mm]	$\boldsymbol{\sigma_{num}}$ [MPa]
UT	31371.7	12	3	871.4

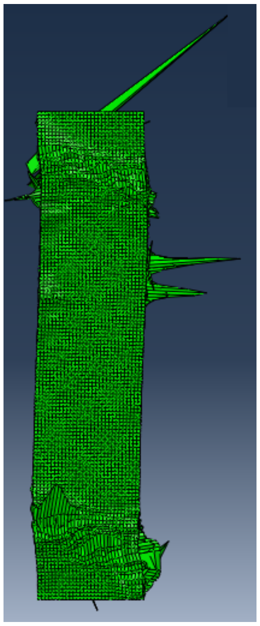

Figure 27: Virtual Unnotched Tension specimen after failure.

It is evident from the figure presented above that some elements suffered excessive distortion; however, the crack initiated and propagated in the bottom, where the elements deform as intended.

After both simulations reached the desirable results, the comparison between numerical and experimental values was done by confronting both ultimate stresses and calculating the resulting relative error, as presented in the table below.

Table 27: Comparison between numerical and experimental values for the unnotched specimens.

Specimen	$\boldsymbol{P^{\infty}}$ [N]	$\boldsymbol{\sigma_{num}}$ [MPa]	$\boldsymbol{\sigma_{exp}}$ [MPa]	relative error [%]
UT	31371.7	871.4	846.1	3.0
UC	19457.3	540.5	532.6	1.5

A graphical representation of the obtained results is presented in the scatter chart below.

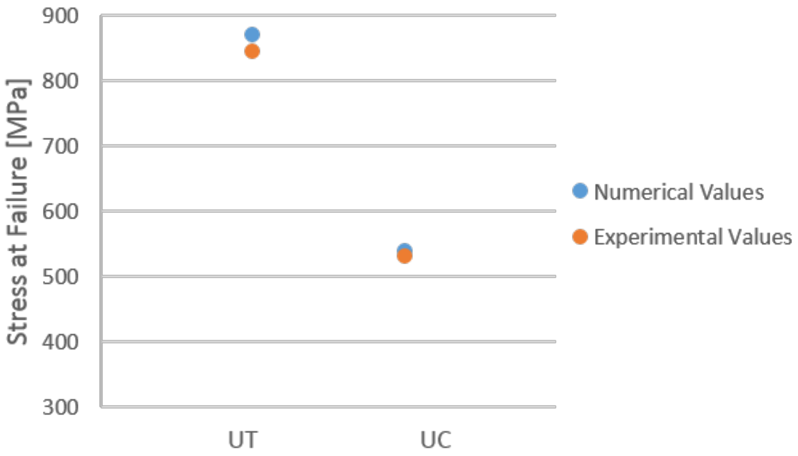

Figure 28: Graphical representation of both numerical and experimental values of the stress at failure for plain strength specimens.

Both the chart in figure 28 and the values in table 27 show that the numerical results approximate very closely the experimental results. However, the simulation over-predicts the remote stress in both loading scenarios.

4.2.2 Open Hole specimens

Routines to simulate the experimental tests of Open Hole specimens were submitted to the cluster. The geometries used for the IM7/8552 specimens were similar to the ones used in the experimental tests in order to allow the comparison of the two results.

In these specimens, two different parts are defined: the support, which is composed of linear elements so as not to increase computation time unnecessarily, and the center part, with the hole, which is composed of damage elements whose properties are based on the SCM and are defined in a material input subroutine. This simplification is possible because it is known in advance that the crack will initiate in the edge of the hole due to high stress concentration.

The specimens were tested stipulating a velocity that is defined by a smooth step amplitude so it ramps up smoothly from one amplitude value to the next [35], as can be seen in figure 29.

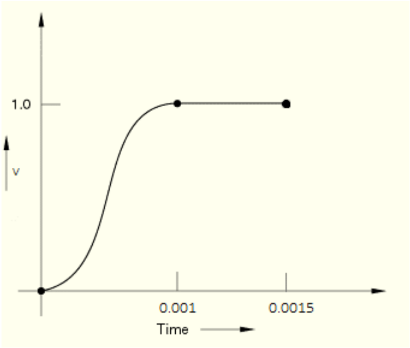

Figure 29: Graphical representation of the variation of the velocity in the simulation of the OHT specimens [35].

For the biggest tensile specimens, the firstly defined 0.0015 value for the simulation time had to be increased to 0.002 in order to permit the conclusion of the test, since no decrease of the load was being accomplished.

4.2.2.1 Compression

Being specimens virtually constructed to mimic the real ones used for the experimental tests, the geometry of the virtual specimens is the same as in the experimental tests and can be remembered in table 28, presented below.

Table 28: Dimensions of the virtual Open Hole Compression specimens.

Specimen	l [mm]	w [mm]	t [mm]	d [mm]
OHC12	300	12	3	2
OHC18	300	18	3	3
OHC24	300	24	3	4
OHC30	300	30	3	5

The models submitted, which took about a day each to run, allowed the attainment of the maximum load that the specimens endured before failing. Having in mind that the input files of the specimens are written evoking symmetry of the specimen, the stress at failure can be obtained by the formula:

$$\boldsymbol{\sigma_{num} = \frac{2P^{\infty}}{wt}}$$

With $\boldsymbol{P}^{\infty}$ as the ultimate load retracted from Abaqus. The comparison between the numerical and the experimental values can be analysed in both table 29 and figure 30.

Table 29: Comparison between numerical and experimental values for the OHC specimens.

Specimen	$\boldsymbol{P}^{\infty}$ [N]	$\boldsymbol{\sigma_{num}}$ [MPa]	$\boldsymbol{\sigma_{exp}}$ [MPa]	relative error [%]
OHC12	7461.2	414.5	383.1	8.2
OHC18	11368.7	421.1	372.9	12.9
OHC24	13961.4	387.8	365.2	6.2
OHC30	17211.1	382.5	353.7	8.1

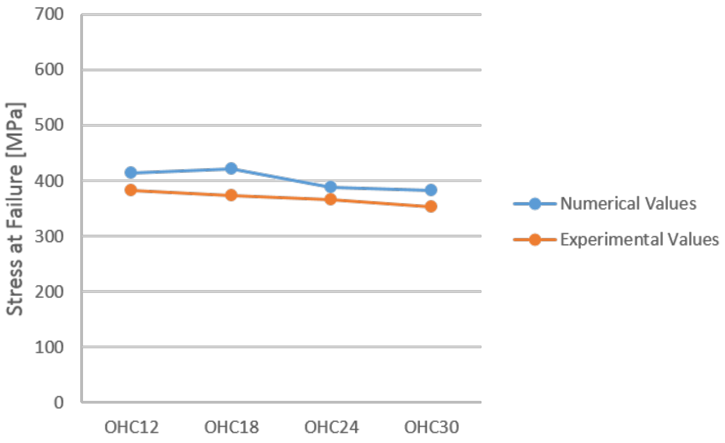

Figure 30: Graphical representation of both numerical and experimental values of the stress at failure for OHC specimens.

All results show a very close approximation of the experimental behaviour of the material under physical testing.

4.2.2.2 Tension

The virtual testing of the OHT specimens is made in the same way as the compression ones, differing only in size since these go up to 60 mm in width. Their geometries can be seen in table 30.

Table 30: Dimensions of the virtual Open Hole Tension specimens.

Specimen	l [mm]	w [mm]	t [mm]	d [mm]
OHT12	200-300	12	3	2
OHT24	200-300	24	3	4
OHT36	200-300	36	3	6
OHT48	200-300	48	3	8
OHT60	200-300	60	3	10

Once the bigger tension specimens required a more prolonged period of time of computation, the last one (OHT60) took up to three days to reach completion using 32 CPU cores. Again, the ultimate load was retrieved from Abaqus and the numerical results were compared to the experimental ones. The table and graphic below allow that comparison.

Table 31: Comparison between numerical and experimental values for the OHT specimens.

Specimen	$\boldsymbol{P^{\infty}}$ [N]	$\boldsymbol{\sigma_{num}}$ [MPa]	$\boldsymbol{\sigma_{exp}}$ [MPa]	relative error [%]
OHT12	11005,3	611,4	555,7	10,0
OHT24	19065,4	529,6	480,6	10,2
OHT36	25588,7	473,9	438,7	8,0
OHT48	31600,9	438,9	375,7	16,8
OHT60	36700,6	407,8	373,7	9,1

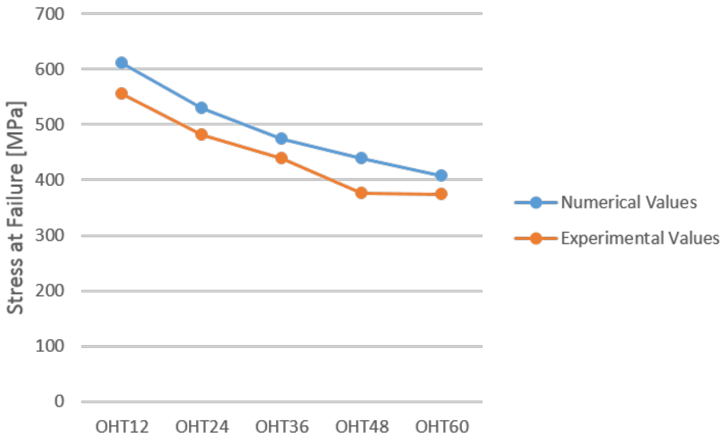

Figure 31: Graphical representation of both numerical and experimental values of the stress at failure for OHT specimens.

As it can be seen in both figures 30 and 31, the simulations always overpredict the amount of applied force that the specimens can endure; however, a relative error of around 10% (always below 17%) is obtained for all simulations, which is significantly lower than the one obtained in previous attempts ([26]) of implementing a structured mesh.

In order to see how the damage variables evolve with the increasing load in the OH specimens, damage maps were developed with Abaqus and can be analysed in Appendix C.

5 Conclusions and Future Work

In the following subsections, the conclusions that can be drawn from the developed work and the improvements that can be performed in the future as a continuation of the work developed in the present thesis are presented.

5.1 Conclusions

The main conclusions of the paper are divided as presented:

- The improvements performed to the VUMAT routine since [26] have allowed for an average of 15% improvement in the Open Hole simulations; the main alterations to emphasise are in the addition of the recently developed Invariant Failure Criteria [14];

- The unnotched specimens resulted in very low relative errors, 3% for the tensile test and 1.5% for the compressive one;

- Changing the velocity, time and mass scaling parameters of the simulation allows for the fine tuning of the routines and can be balanced to find the optimal results without greatly increasing computation time;

- For the Open Hole Compression specimens, a decreasing value of the ultimate stress is obtained when the hole diameter increases, even though $\frac{w}{d}$ is kept constant at 6, which is in agreement with the experimental results. The only discrepancy is found with the Open Hole Compression (OHC18) specimen that shows a slight increase in stress from the specimen in the level behind it; however, even in the experimental tests, the decreasing tendency is of small magnitude;

- The largest OHT specimens took a very long time to simulate, when compared to the smaller ones or the compression ones, a fact that can easily be explained by the increase in the number of elements from around 30 000 to 800 000; to be noted that, already, only half of the specimen was simulated in an effort to reduce computational time;

- In all of the OHC simulations, the specimens presented at least an element with excessive distortion while in the tensile tests, only the biggest specimen (w=60 mm) presented excessive distortion; it is visible from the damage figures that the compressive tests are much more destructive;

- Even tough the loading of the unnotched specimens may seem very straightforward, the lack of crack or notch leads to a very unpredictable failure behaviour.

5.2 Future Work

The future work recommended is:

- Continuation of the validation of the rest of the developed routines with the help of the enumerated experimental tests already performed;
- To make sure that the crack in the unnotched specimens initiates in the middle of the specimen, the .inp file could be altered in order to develop the part with three different components: the supports with elements with an elastic behaviour and the centre of the specimen with elements whose behaviour are based in the models presented in the thesis;
- Test unnotched specimens with an off-axis loading and study the effect of fibre direction simulated in the structured mesh;
- Submit again the OHC18 routine, in an attempt to capture the scale law, after rearranging the pertinent parameters;
- In an attempt to minimize the relative error, OHT48 could be tested again after adjusting the mass scaling and velocity parameters.

Appendix A

Damage Evolution Criterion in tabular form

```
*Damage Evolution, type=ENERGY, mixed mode behavior=TABULAR,
mode mix ratio=TRACTION 0.28,0,0
0.280000832,0.006430284,0
0.280006394,0.012990437,0
0.28002133,0.019682997,0
0.280050567,0.026510489,0
0.280099413,0.033475417,0
0.280173611,0.040580253,0
0.280279381,0.047827433,0
0.280423451,0.055219341,0
0.280613089,0.062758304,0
0.280856131,0.070446575,0
0.281160997,0.078286324,0
0.281536717,0.086279622,0
0.28199294,0.094428432,0
0.282539949,0.102734586,0
0.28318866,0.111199776,0
0.283950624,0.119825532,0
0.284838013,0.128613209,0
0.285863608,0.137563966,0
0.287040764,0.146678746,0
0.288383382,0.155958261,0
0.28990585,0.165402965,0
0.291622991,0.175013041,0
0.293549983,0.184788375,0
0.295702275,0.194728537,0
0.298095483,0.204832765,0
0.300745276,0.215099935,0
0.303667242,0.225528553,0
0.306876746,0.236116728,0
0.310388768,0.246862159,0
0.314217732,0.257762117,0
0.318377325,0.268813433,0
0.3228803,0.280012485,0
0.327738279,0.291355186,0
0.332961549,0.302836982,0
0.338558855,0.314452842,0
```

```
0.344537197,0.326197262,0
0.350901635,0.338064264,0
0.357655105,0.350047408,0
0.364798245,0.362139794,0
0.372329249,0.374334084,0
0.38024374,0.386622514,0
0.388534671,0.398996923,0
0.397192263,0.411448773,0
0.406203975,0.423969184,0
0.415554509,0.436548965,0
0.425225865,0.449178653,0
0.435197425,0.461848552,0
0.445446087,0.474548777,0
0.455946431,0.487269302,0
0.466670926,0.5,0
0.477590172,0.512730698,0
0.488673167,0.525451223,0
0.499887603,0.538151448,0
0.511200177,0.550821347,0
0.52257692,0.563451035,0
0.533983527,0.576030816,0
0.545385691,0.588551227,0
0.556749429,0.601003077,0
0.568041398,0.613377486,0
0.579229188,0.625665916,0
0.590281601,0.637860206,0
0.601168896,0.649952592,0
0.611863007,0.661935736,0
0.622337732,0.673802738,0
0.632568885,0.685547158,0
0.642534412,0.697163018,0
0.65221448,0.708644814,0
0.661591529,0.719987515,0
0.670650291,0.731186567,0
0.679377783,0.742237883,0
0.687763274,0.753137841,0
0.695798229,0.763883272,0
0.703476222,0.774471447,0
0.710792853,0.784900065,0
0.717745626,0.795167235,0
```

0.724333834,0.805271463,0
0.73055843,0.815211625,0
0.73642189,0.824986959,0
0.741928074,0.834597035,0
0.74708209,0.844041739,0
0.751890156,0.853321254,0
0.756359466,0.862436034,0
0.760498057,0.871386791,0
0.764314689,0.880174468,0
0.767818723,0.888800224,0
0.771020015,0.897265414,0
0.773928808,0.905571568,0
0.776555638,0.913720378,0
0.778911248,0.921713676,0
0.781006508,0.929553425,0
0.782852342,0.937241696,0
0.784459665,0.944780659,0
0.785839328,0.952172567,0
0.787002065,0.959419747,0
0.787958453,0.966524583,0
0.788718871,0.973489511,0
0.789293473,0.980317003,0
0.78969216,0.987009563,0
0.789924558,0.993569716,0
0.79,1,0

Appendix B

Load-time charts

After the simulation of the Open-Hole and the Unnotched specimens, the results were analysed with the help of the load-time charts presented below.

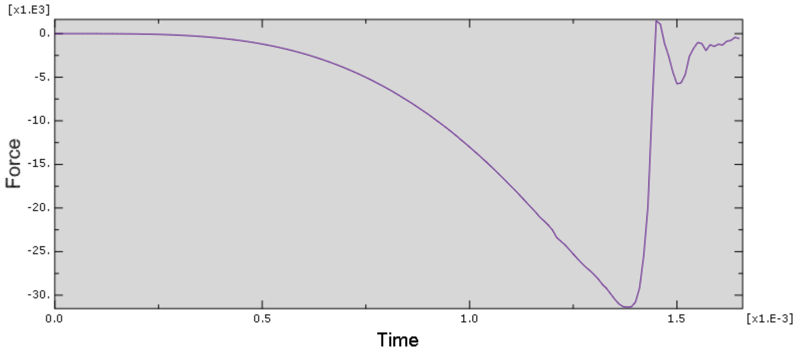

Figure 32: Graphical representation of load evolution for the UT specimen.

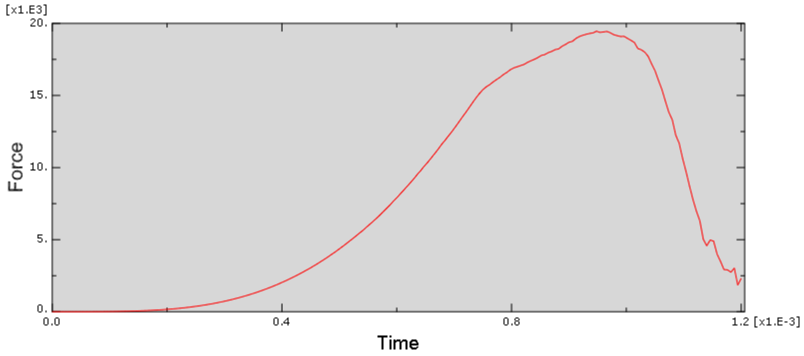

Figure 33: Graphical representation of load evolution for the UC specimen.

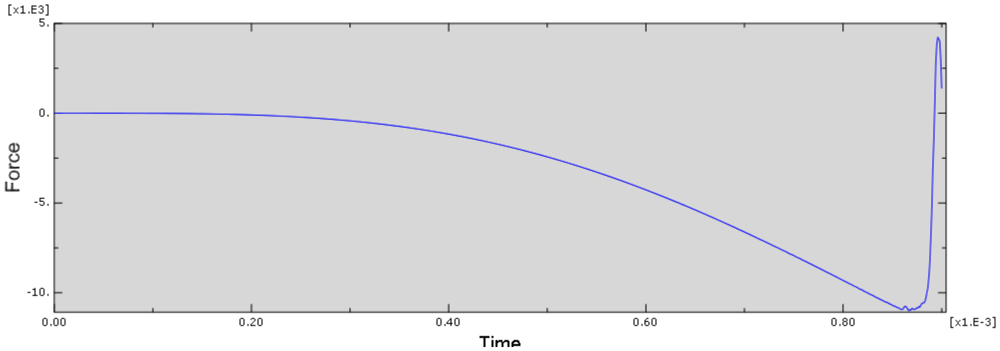

Figure 34: Graphical representation of load evolution for the OHT12 specimen.

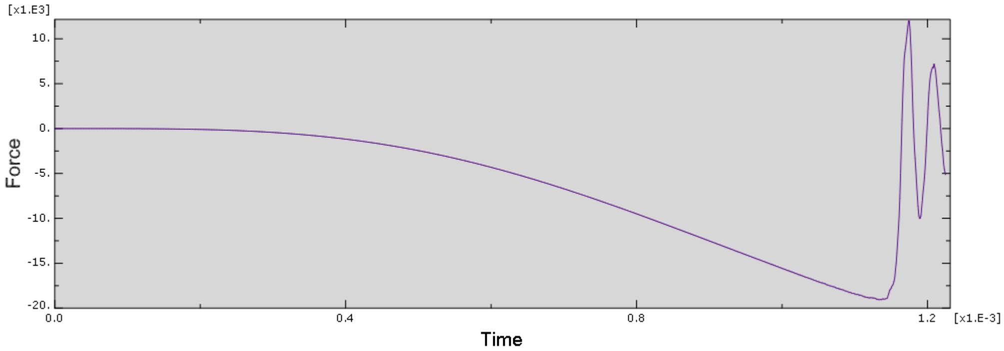

Figure 35: Graphical representation of load evolution for the OHT24 specimen.

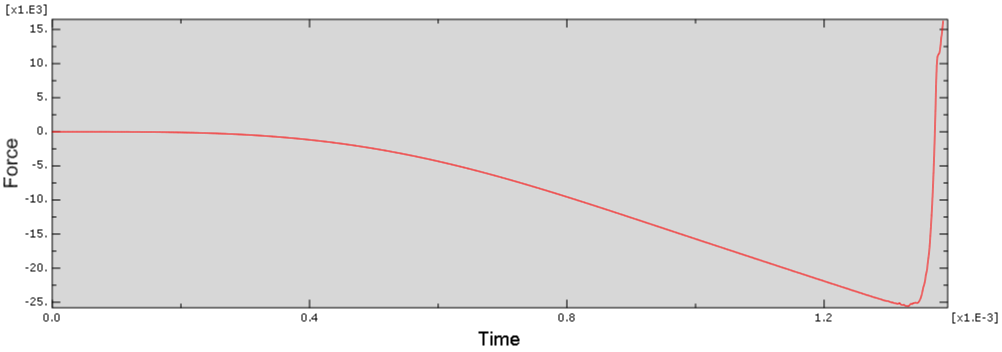

Figure 36: Graphical representation of load evolution for the OHT36 specimen.

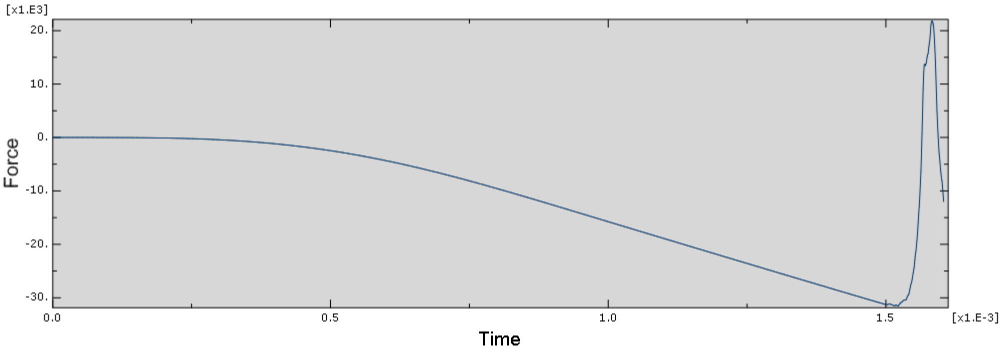

Figure 37: Graphical representation of load evolution for the OHT48 specimen.

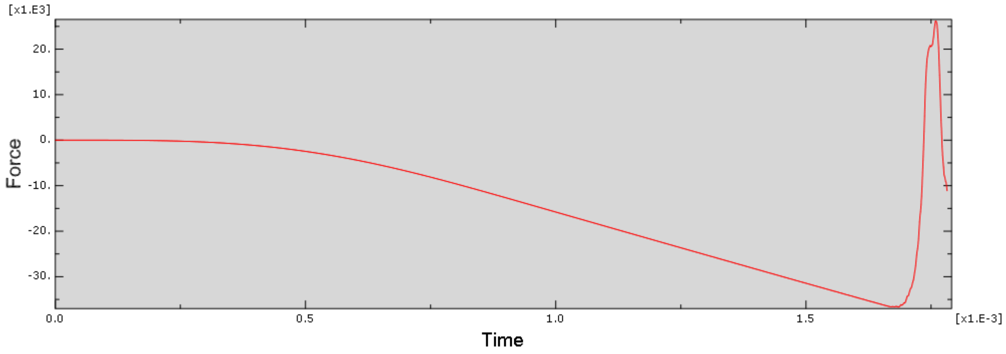

Figure 38: Graphical representation of load evolution for the OHT60 specimen.

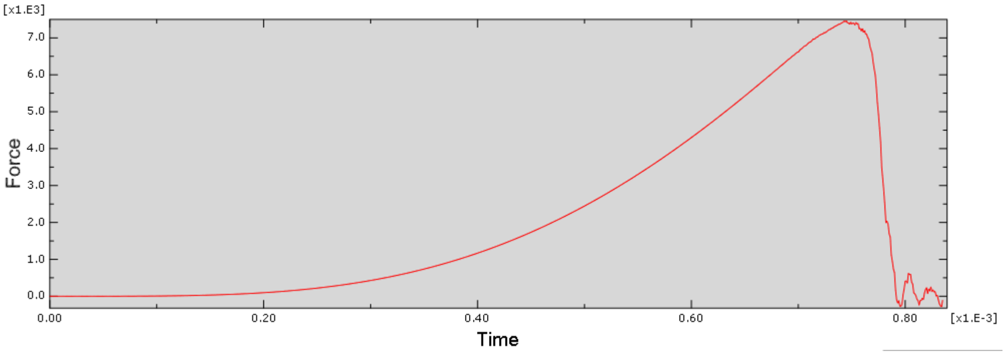

Figure 39: Graphical representation of load evolution for the OHC12 specimen.

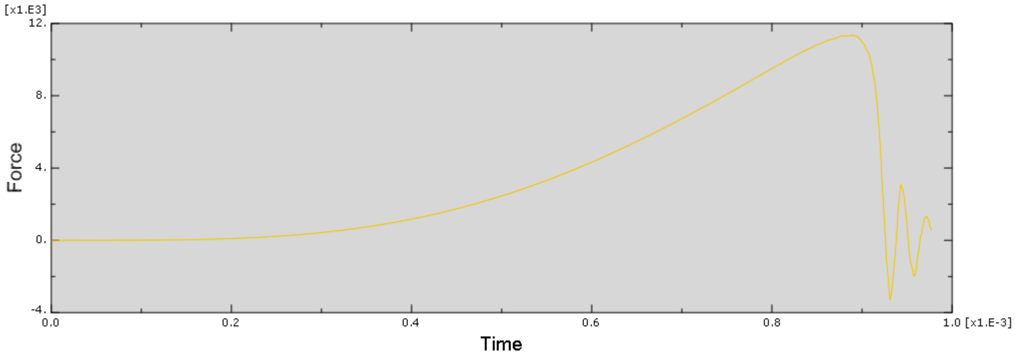

Figure 40: Graphical representation of load evolution for the OHC18 specimen.

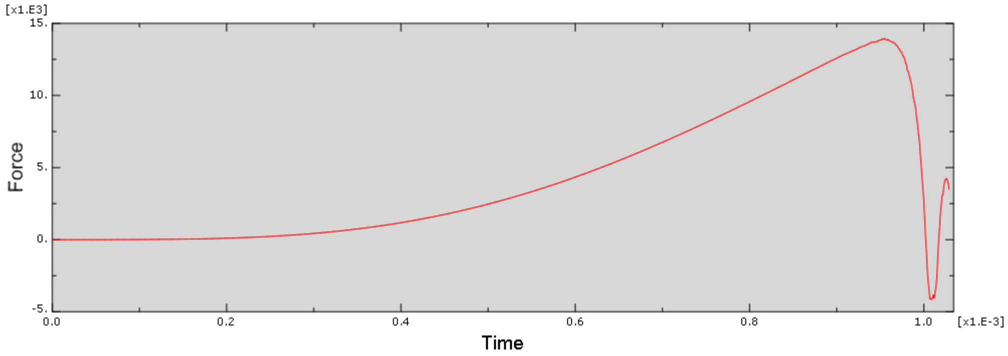

Figure 41: Graphical representation of load evolution for the OHC24 specimen.

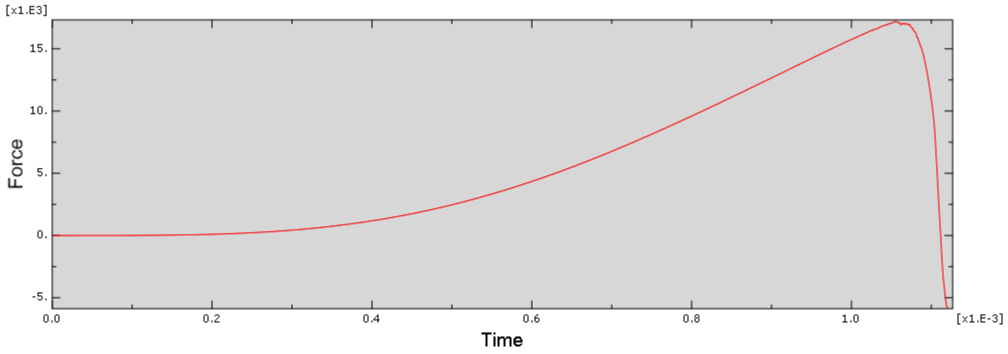

Figure 42: Graphical representation of load evolution for the OHC30 specimen.

Appendix C

Damage Maps

Damage Maps of the $\boldsymbol{d_2}$ variable were obtained for the $\mathbf{90°}$, $\mathbf{0°}$, $\mathbf{+45°}$ and $\mathbf{-45°}$ plies of the smallest and the largest of the OHT specimens - OHT12 and OHT60 respectively.

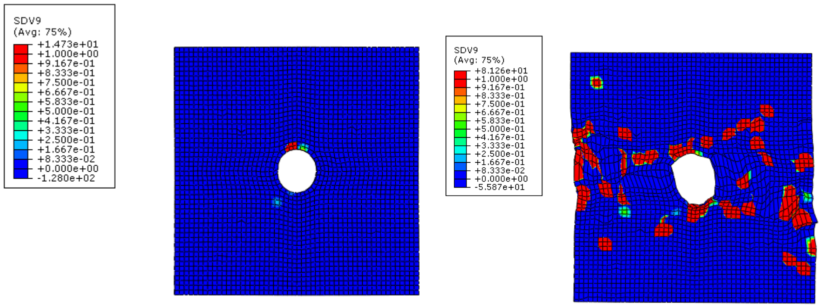

(a) Damage initiation.

(b) Damage at peak load.

Figure 43: Damage maps of the $\boldsymbol{d_2}$ variable at the $\mathbf{90°}$ ply of the OHT12 specimen.

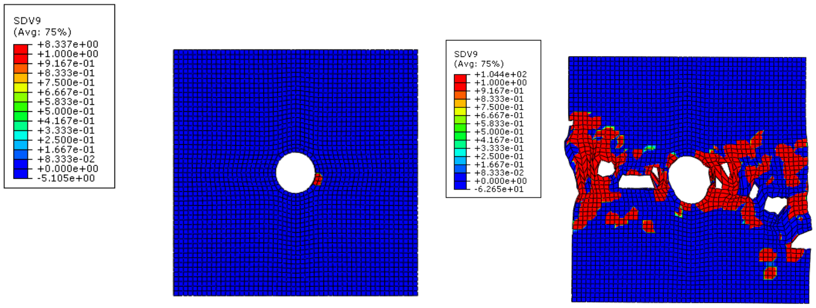

(a) Damage initiation.

(b) Damage at peak load.

Figure 44: Damage maps of the $\boldsymbol{d_2}$ variable at the $\mathbf{0°}$ ply of the OHT12 specimen.

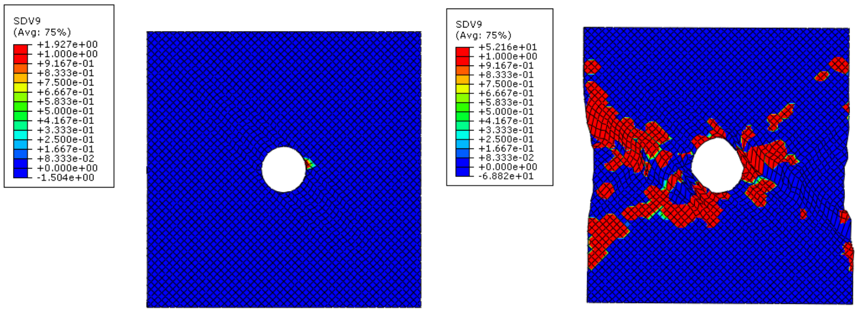

(a) Damage initiation.

(b) Damage at peak load.

Figure 45: Damage maps of the $\boldsymbol{d_2}$ variable at the $\boldsymbol{+45^\circ}$ ply of the OHT12 specimen.

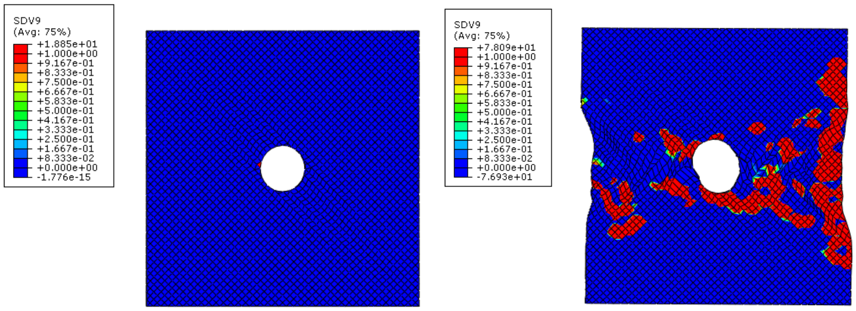

(a) Damage initiation.

(b) Damage at peak load.

Figure 46: Damage maps of the $\boldsymbol{d_2}$ variable at the $\boldsymbol{-45^\circ}$ ply of the OHT12 specimen.

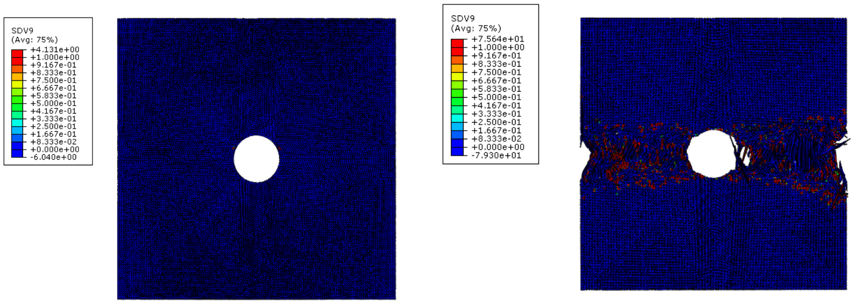

(a) Damage initiation.

(b) Damage at peak load.

Figure 47: Damage maps of the $\boldsymbol{d_2}$ variable at the **90°** ply of the OHT60 specimen.

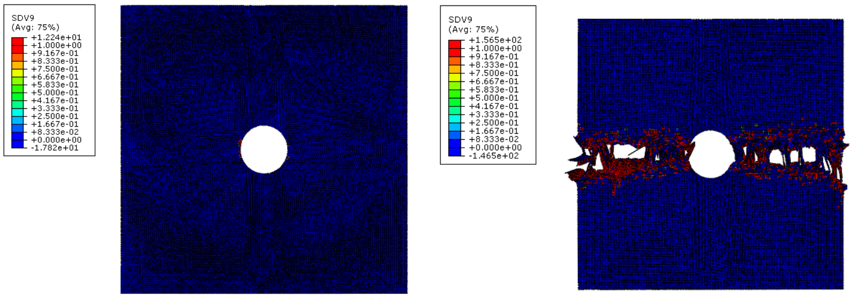

(a) Damage initiation.

(b) Damage at peak load.

Figure 48: Damage maps of the $\boldsymbol{d_2}$ variable at the **0°** ply of the OHT60 specimen.

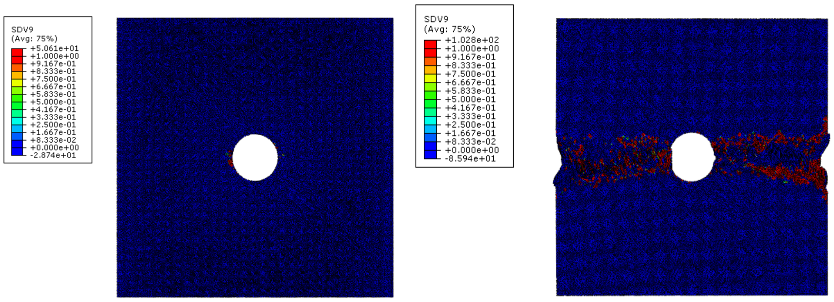

(a) Damage initiation. (b) Damage at peak load.

Figure 49: Damage maps of the $\boldsymbol{d_2}$ variable at the $\boldsymbol{+45°}$ ply of the OHT60 specimen.

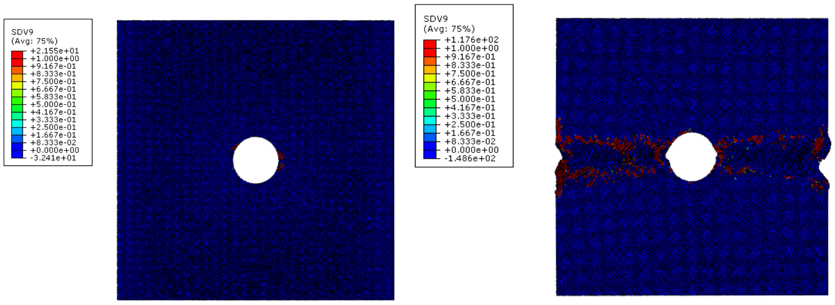

(a) Damage initiation. (b) Damage at peak load.

Figure 50: Damage maps of the $\boldsymbol{d_2}$ variable at the $\boldsymbol{-45°}$ ply of the OHT60 specimen.

For the compression specimens, damage maps were equally obtained in Abaqus for the $\boldsymbol{d_2}$ variable for all ply orientations and for the $\boldsymbol{d_1}$ at the $\boldsymbol{0°}$ ply. Once again, these plots were produced for the smallest and largest specimens, OHC12 and OHC30.

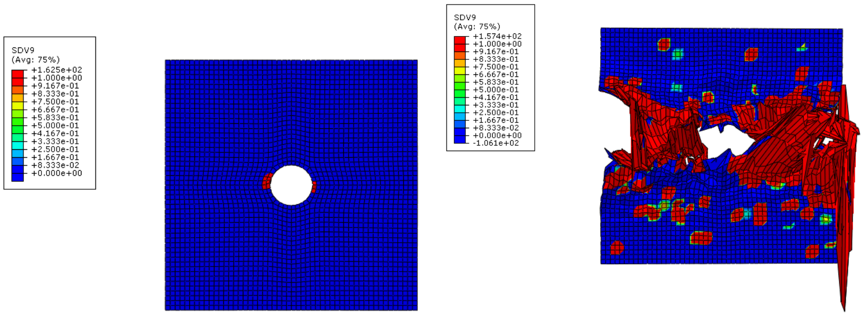

(a) Damage initiation. (b) Damage at peak load.

Figure 51: Damage maps of the $\boldsymbol{d_2}$ variable at the $\mathbf{90°}$ ply of the OHC12 specimen.

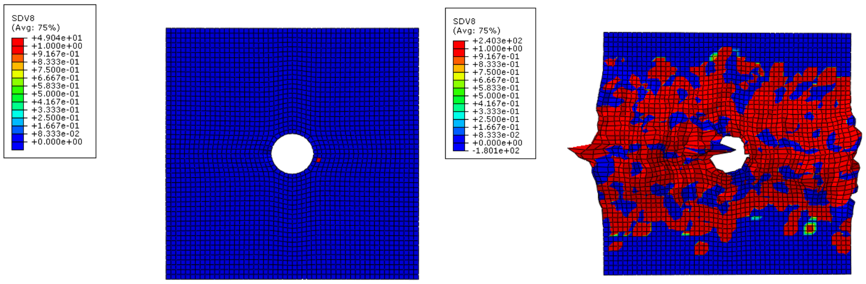

(a) Damage initiation. (b) Damage at peak load.

Figure 52: Damage maps of the $\boldsymbol{d_1}$ variable at the $\mathbf{0°}$ ply of the OHC12 specimen.

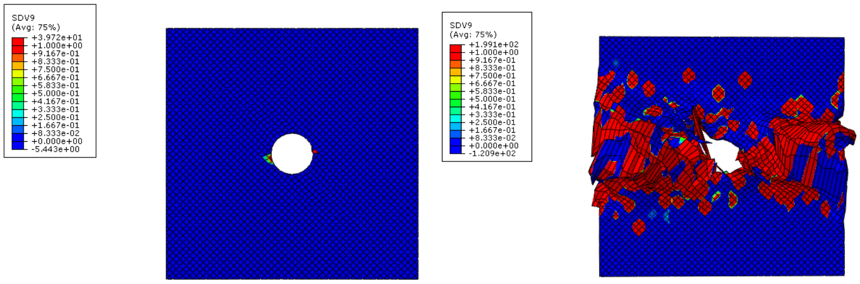
(a) Damage initiation.
(b) Damage at peak load.

Figure 53: Damage maps of the $\boldsymbol{d_2}$ variable at the $\mathbf{+45°}$ ply of the OHC12 specimen.

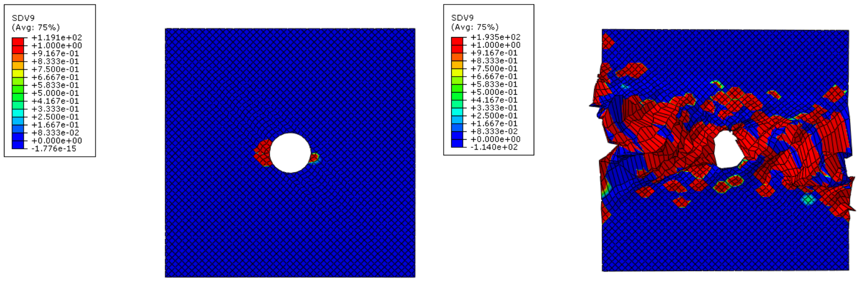
(a) Damage initiation.
(b) Damage at peak load.

Figure 54: Damage maps of the $\boldsymbol{d_2}$ variable at the $\mathbf{-45°}$ ply of the OHC12 specimen.

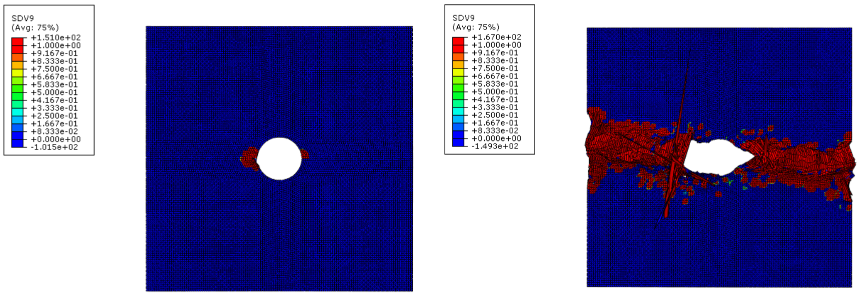
(a) Damage initiation.
(b) Damage at peak load.

Figure 55: Damage maps of the $\boldsymbol{d_2}$ variable at the $\mathbf{90°}$ ply of the OHC30 specimen.

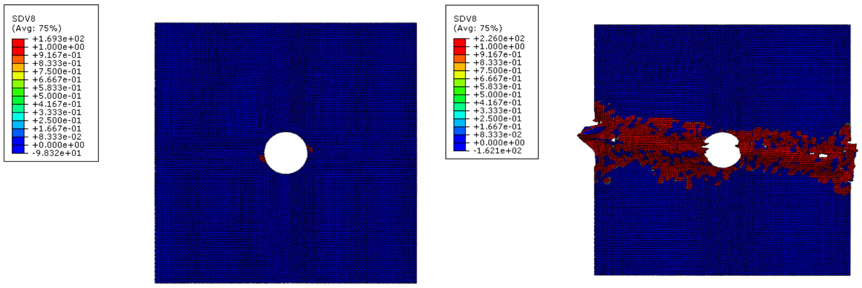

(a) Damage initiation.

(b) Damage at peak load.

Figure 56: Damage maps of the $\boldsymbol{d_1}$ variable at the $\mathbf{0°}$ ply of the OHC30 specimen.

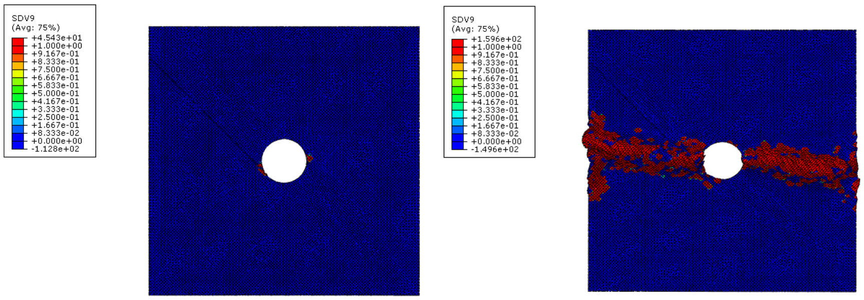

(a) Damage initiation.

(b) Damage at peak load.

Figure 57: Damage maps of the $\boldsymbol{d_2}$ variable at the $\mathbf{+45°}$ ply of the OHC30 specimen.

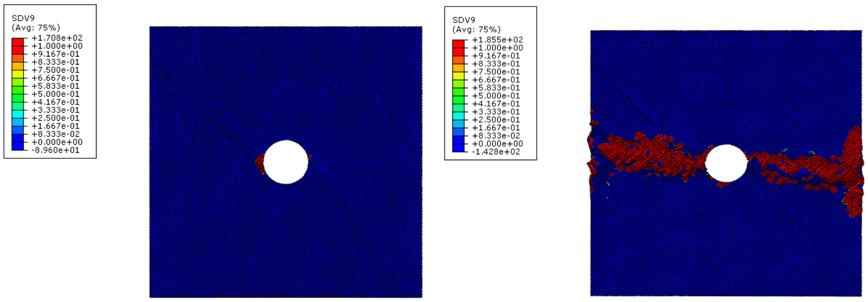

(a) Damage initiation.

(b) Damage at peak load.

Figure 58: Damage maps of the $\boldsymbol{d_2}$ variable at the $\boldsymbol{-45^\circ}$ ply of the OHC30 specimen.

References

[1] ESAComp3.5 Commercial software.

[2] American Society for Testing and Materials (ASTM). Standard Test Method for Mode I Interlaminar Fracture Toughness of Unidirectional. *Annual Book of ASTM 03* (2004), 1–12.

[3] American Society for Testing and Materials (ASTM). Standard Test Method for In-Plane Shear Response of Polymer Matrix Composite Materials by Tensile Test of a 45 Laminate. *Annual Book of ASTM 94*, Reapproved (2007), 1–7.

[4] American Society for Testing and Materials (ASTM). Standard Test Method for Compressive Properties of Polymer Matrix Composite Materials with Unsupported Gage Section by Shear Loading - ASTM D3410, 2008.

[5] American Society for Testing and Materials (ASTM). Standard Test Method for Open-Hole Tensile Strength of Polymer Matrix Composite Laminates - ASTM D5766, 2011.

[6] American Society for Testing and Materials (ASTM). Standard Test Method for Bearing Response of Polymer Matrix Composite Laminates - ASTM D5961, 2013.

[7] American Society for Testing and Materials (ASTM). Standard Test Method for Open-Hole Compressive Strength of Polymer Matrix Composite Laminates - ASTM D6484 / D6484M, 2014.

[8] American Society for Testing and Materials (ASTM). Standard test method for tensile properties of polymer matrix composite materials - ASTM D3039/D3039M, 2014.

[9] Argon, A. S. Fracture of Composites. In *Treatise on Materials Science and Technology*, A. Press, Ed., 1 ed. New York, 1972.

[10] Aronsson, C., and Backlund, J. Tensile fracture of laminates with cracks. *Journal of composite materials, American Society for Composites* (1986).

[11] Arteiro, A. Technology development and structural mechanics of composites built of spread tow thin-ply technology. 2012.

[12] Bažant, Z., and Oh, B. Crack band theory for fracture of concrete. *Materials and Structures* (1983).

[13] Benzeggagh, M. L., and Kenane, M. Measurement of mixed-mode delamination fracture toughness of unidirectional glass/epoxy composites with mixed-mode bending apparatus. *Composites Science and Technology 56* (1996), 439–449.

[14] Camanho, P. P., Arteiro, a., Melro, a. R., Catalanotti, G., and Vogler, M. Three-dimensional invariant-based failure criteria for fibre-reinforced composites. *International Journal of Solids and Structures 55* (2014), 92–107.

[15] Camanho, P. P., Bessa, M. A., Catalanotti, G., Vogler, M., and Rolfes, R. Modeling the inelastic deformation and fracture of polymer composites-Part II: Smeared crack model. *Mechanics of Materials 59* (2013), 36–49.

[16] Camanho, P. P., and Catalanotti, G. On the relation between the mode I fracture toughness of a composite laminate and that of a 0 ply: Analytical model and experimental validation. *Engineering Fracture Mechanics 78*, 13 (2011), 2535–2546.

[17] Camanho, P. P., and Lambert, M. A design methodology for mechanically fastened joints in laminated composite materials. *Composites Science and Technology 66* (2006), 3004–3020.

[18] Camanho, P. P., Maimí, P., and Dávila, C. G. Prediction of size effects in notched laminates using continuum damage mechanics. *Composites Science and Technology 67* (2007), 2715–2727.

[19] Catalanotti, G., Arteiro, A., Hayati, M., and Camanho, P. P. Determination of the mode I crack resistance curve of polymer composites using the size-effect law. *Engineering Fracture Mechanics 118* (2014), 49–65.

[20] Catalanotti, G., Camanho, P. P., and Marques, a. T. Three-dimensional failure criteria for fiber-reinforced laminates. *Composite Structures 95* (2013), 63–79.

[21] Catalanotti, G., Camanho, P. P., Xavier, J., Dávila, C. G., and Marques, a. T. Measurement of resistance curves in the longitudinal failure of composites using digital image correlation. *Composites Science and Technology 70*, 13 (2010), 1986–1993.

[22] Catalanotti, G., Xavier, J., and Camanho, P. P. Measurement of the compressive crack resistance curve of composites using the size effect law. *Composites Part A: Applied Science and Manufacturing 56* (2014), 300–307.

[23] Davila, C. G., Camanho, P. P., and Rose, C. A. Failure Criteria for FRP Laminates in Plane Stress.

[24] Dávila, C. G., Rose, C. A., and Iarve, E. Modeling Fracture and Complex Crack Networks in Laminated Composites. 2011, pp. 1–56.

[25] D.S. Simulia. *Abaqus 6.14 Online Documentation*. 2014.

[26] Erçin, G. H. *Stress Gradient Effects in Laminated Composites*. PhD thesis, 2013.

[27] Jackson, W., and Ratcliffe, J. Measurement of fracture energy for kink-band growth in sandwich specimens. *Composites Testing and Model Identification, CompTest2004, University of Bristol, Bristol, UK*, Paper no. 24 (2004).

[28] Jirásek, M., and Grassl, P. Evaluation of directional mesh bias in concrete fracture simulations using continuum damage models. *Engineering Fracture Mechanics 75* (2008), 1921–1943.

[29] Laffan, M. J., Pinho, S. T., Robinson, P., and Iannucci, L. Measurement of the in situ ply fracture toughness associated with mode I fibre tensile failure in FRP. Part I: Data reduction. *Composites Science and Technology 70*, 4 (2010), 606–613.

[30] Maimí, P., Camanho, P. P., Mayugo, J. A., and Dávila, C. G. A continuum damage model for composite laminates: Part I - Constitutive model. *Mechanics of Materials 39* (2007), 897–908.

[31] Maimí, P., Camanho, P. P., Mayugo, J. A., and Dávila, C. G. A continuum damage model for composite laminates: Part II - Computational implementation and validation. *Mechanics of Materials 39* (2007), 909–919.

[32] Martin, R. H. ., Elms, T., and Bowron, S. Characterisation of mode II delamination using the 4 ENF. *4 th European Conference on Composites: Testing and Standardisation* (1998), 161–170.

[33] Pinho, S. T., Davilla, C. G., Camanho, P. P., Iannucci, L., and Robinson, P. Failure Models and Criteria for FRP Under In-Plane or Three-Dimensional Stress States Including Shear Non-Linearity.

[34] Pinho, S. T., Robinson, P., and Iannucci, L. Fracture toughness of the tensile and compressive fibre failure modes in laminated composites. *Composites Science and Technology 66* (2006), 2069–2079.

[35] Simulia. Obtaining Improved Results in Abaqus Mixed Mode Fracture Simulations Using Cohesive Elements or Surfaces. 2–4.

[36] Song, K., Dávila, C. G., and Rose, C. A. Guidelines and parameter selection for the simulation of progressive delamination. *abaqus User's Conference, Newport, ...* (2008), 1–15.

[37] Soutis, C., and Fleck, N. Static Compression Failure of Carbon Fibre T800/924C Composite Plate with a Single Hole. *Journal of Composite Materials 24*, 5 (1990), 536–558.

[38] Tijssens, M. G. a., Sluys, B. L. J., and Van der Giessen, E. Numerical simulation of quasi-brittle fracture using damaging cohesive surfaces. *European Journal of Mechanics, A/Solids 19* (2000), 761–779.

[39] Turon, A., Camanho, P. P., Costa, J., and Dávila, C. G. A damage model for the simulation of delamination in advanced composites under variable-mode loading. *Mechanics of Materials 38* (2006), 1072–1089.

[40] Vogler, M., Rolfes, R., and Camanho, P. P. Modeling the inelastic deformation and fracture of polymer composites-Part I: Plasticity model. *Mechanics of Materials 59* (2013), 50–72.

[41] Zhang, C., Binienda, W. K., and Goldberg, R. K. Free-edge effect on the effective stiffness of single-layer triaxially braided composite. *Composites Science and Technology 107* (2015), 145–153.

[42] Zhang, J., and Zhang, X. Simulating low-velocity impact induced delamination in composites by a quasi-static load model with surface-based cohesive contact. *Composite Structures 125* (2015), 51–57.